

PASSIVELY COMPLIANT MEMBRANES IN LOW ASPECT RATIO WINGS

By

MANUEL ALEX ARCE

A THESIS PRESENTED TO THE GRADUATE SCHOOL  
OF THE UNIVERSITY OF FLORIDA IN PARTIAL FULFILLMENT  
OF THE REQUIREMENTS FOR THE DEGREE OF  
MASTER OF SCIENCE

UNIVERSITY OF FLORIDA

2013

© 2013 Manuel Alex Arce

To Dawn

## ACKNOWLEDGMENTS

I would like to thank Dr. Lawrence Ukeiley for his support and guidance throughout my research. Many thanks to my other committee members, Dr. Peter Ifju and Dr. Rick Lind, for reviewing my work and their valuable feedback. I would also like to thank all of my office mates for their respected inputs and daily discussions both in and out of the office. A special thanks goes to Amory Timpe for spending his limited time showing me the basics of his research. Additional thanks to Yaakov Abudararm, for creating the membrane models used throughout this study. I would also like to thank the support provided by the Air Force Office of Scientific Research under program manager Dr. Doug Smith, the Florida Center for Advanced Aero Propulsion, and the Air Force Research Lab's Munitions Directorate. A special thank you to my family, without their love and support I would not be where I am today, you guys are truly the best. Finally I want to thank Natalie Andrietta, for her endless amount of support while putting up with the long nights and short weekends.

## TABLE OF CONTENTS

	<u>page</u>
ACKNOWLEDGMENTS.....	4
LIST OF TABLES.....	7
LIST OF FIGURES.....	8
LIST OF ABBREVIATIONS.....	10
ABSTRACT.....	11
CHAPTER	
1 INTRODUCTION.....	13
Motivation.....	13
Background.....	14
Previous Investigations.....	14
Predecessor Investigations.....	19
Current Investigations.....	21
2 FACILITIES AND EXPERIMENTAL SETUP.....	23
Facilities.....	23
Aerodynamic Characterization Facility.....	23
Engineering Laboratory Design Wind Tunnel.....	24
Models.....	24
Experimental Equipment.....	25
Particle Image Velocimetry.....	26
Digital Image Correlation.....	27
Synchronization.....	28
Experimental Description.....	29
Synchronized PIV and DIC.....	29
Independent DIC.....	30
Post-Processing.....	31
PIV.....	31
DIC and PIV.....	32
3 RESULTS AND DISCUSSION.....	39
Flow-Field Measurements.....	39
Membrane Surface Deflections.....	43
Mean and Root Mean Square Deflections.....	44
Effects of Mounting Hardware.....	45
Mean and Root Mean Square Deflections Along the Mid-Plane.....	46

Power Spectral Density and Membrane Motion .....	47
Wave Speed.....	50
Fluid Structure Interactions .....	52
4 SUMMARY AND FUTURE WORK .....	75
Summary .....	75
Future Investigation .....	77
<b>APPENDIX</b>	
A 2D PIV UNCERTAINTY .....	79
B VIBRATIONAL ANALYSIS.....	80
LIST OF REFERENCES .....	83
BIOGRAPHICAL SKETCH.....	88

## LIST OF TABLES

<u>Table</u>		<u>page</u>
2-1	Membrane's properties.....	36
2-2	BR membrane model dimensions.....	36

## LIST OF FIGURES

<u>Figure</u>	<u>page</u>
1-1 Flexible membrane MAVs .....	22
2-1 Low speed test facilities.....	33
2-2 Linear relation between temperature of creation and measured pre-strain .....	34
2-3 Measured pre-strain within the membranes .....	34
2-4 Aspect ratio 2 membrane models and flat plate model.....	35
2-5 Membrane wing nomenclature .....	35
2-6 Statistical convergences for the 1 percent pre-tension membrane model at 16° AoA .....	36
2-7 Combined fields of view from PIV cameras.....	37
2-8 Digital inclinometer on top of model.....	37
2-9 Experimental set-up.....	38
2-10 Membrane model with center supported hardware positioned within the ELD-WT.....	38
3-1 Normalized mean U-component of the flow-field with streamlines for the different models.....	55
3-2 Normalized Urms contours for the different models.....	56
3-3 Normalized RSS for the different models .....	57
3-4 Normalized instantaneous vorticity for the 1 percent pre-tension membrane at 20° AoA .....	58
3-5 Normalized mean membrane deflections and normalized RMS deflections through a range of AoAs for the synchronized data.....	59
3-6 Normalized mean membrane deflections and normalized RMS deflections through a range of AoAs for the Independent DIC data with outer supported models.....	60
3-7 Normalized mean membrane deflections and normalized RMS deflections through a range of AoAs for the Independent DIC data with center supported models.....	61

3-8	Membrane's center normalized mean and RMS deflections vs. AoA .....	62
3-9	Time averaged mean camber of middle membrane for the synchronized data. ....	63
3-10	Time averaged mean camber of middle membrane for the independent DIC data .....	63
3-11	Trailing edge PSD for each membrane .....	64
3-12	First dominate frequency vs. AoA for each membrane during synchronized testing.....	65
3-13	First dominate frequency vs. AoA for each membrane during independent DIC testing.....	66
3-14	Instantaneous trailing edge membrane surface deflections for the 1 percent pre-tension membrane model.....	67
3-15	Instantaneous center chord membrane surface deflections for the 1 percent pre-tension membrane model.....	68
3-16	PSD in the spatial domain .....	69
3-17	Cross correlations between spatial locations for the 1 percent pre-tension membrane at 8° AoA .....	70
3-18	Membrane oscillations for the 1 percent pre-tension model at 12° AoA .....	71
3-19	Middle cell average wave speed vs. AoA for both membrane models.....	71
3-20	PSD of both the middle membrane's trailing edge and select locations of the flow-field for the 1 percent pre-tension membrane at 8° AoA .....	72
3-21	PSD of both DIC and PIV for the 1 percent pre-tension membrane model.....	73
3-22	Modified Strouhal number vs. AoA .....	74
B-1	Accelerometer attached to the back of mounting arm .....	81
B-2	PSD of original mounting arm.....	81
B-3	PSD of ELD-WT .....	82
B-4	PSD of cantilevered mounting arm .....	82

## LIST OF ABBREVIATIONS

ACF	Aerodynamic Characterization Facility
AoA(s); $\alpha$	Angle of Attack(s)
AR	Aspect Ratio
BR	Batten Reinforced
DFT	Discrete Fourier Transform
DIC	Digital Image Correlation
ELD-WT	Engineering Laboratory Design Wind Tunnel
FOV	Field of View
FSI	Fluid-Structure Interaction
IA	Interrogation Area
LCO	Limit Cycle Oscillation
MAV(s)	Micro Air Vehicle(s)
PIV	Particle Image Velocimetry
PR	Perimeter Reinforced
PSD	Power Spectral Density
REEF	Research and Engineering Education Facility
RSS	Reynolds Shear Stress
RMS	Root Mean Square
St	Strouhal Number
1D	One Dimensional
2D	Two Dimensional
3D	Three Dimensional

Abstract of Thesis Presented to the Graduate School  
of the University of Florida in Partial Fulfillment of the  
Requirements for the Degree of Master of Science

## PASSIVELY COMPLIANT MEMBRANES IN LOW ASPECT RATIO WINGS

By

Manuel Alex Arce

December 2013

Chair: Lawrence S. Ukeiley  
Major: Aerospace Engineering

The study of mammalian flight has led to the design of bio inspired micro air vehicles. These micro air vehicles utilize passively compliant membranes to help aid in their aerodynamic performance such as flight in unsteady wind conditions. While there has been previous investigations into membrane wings there is still much that is not fully understood of the coupling between the membrane and the flow. The present study examines the fluid structure interactions of an aspect ratio 2, batten reinforced, silicone rubber membrane wing. The membranes are configured to have a free trailing edge and are scalloped by approximately 25% of the chord length; membrane geometry is based off of previous research. To further understand the effects the membranes have on the surrounding flow-field, two different membrane models are tested. The two membrane models consisted of a one percent pre-tension membrane and a four percent pre-tension membrane. The fluid structure interactions are obtained through the use of synchronized time resolved particle image velocimetry and digital image correlation. These two systems measure the two dimensional flow-field and the three dimensional surface deformations respectively. When compared to a rigid flat plate the membrane wings shear layer remained closer to the membrane's surface producing a smaller

separation bubble and decrease in wake deficit. The results show the membrane's motion ability to drive the flow to alter the wake behavior which is typically linked to higher aerodynamic efficiency. Additionally shown, the frequency of the membrane's motion, which is a combination of a standing wave and traveling wave, is translated to the flow and can be altered by changing the pre-tension in the membrane.

## CHAPTER 1 INTRODUCTION

### **Motivation**

The study of natural flyers has been conducted by numerous researchers to provide meaningful analysis into the unique kinematic and aerodynamic capabilities which they possess [1]–[5]. One key feature of several natural flyers involves the use of a flexible wing consisting of a membrane. Mammals with membrane wings, such as bats, operate in a low Reynolds Number regime ( $10^4 - 10^5$ ) based off of their wing chord length and fly at airspeed typically less than 10m/s [2], [3], [6]. These compliant wing natural flyers have a high degree of maneuverability and are able to fly in wind gusts on the order of their flight speed [4], [7]. With flight conditions similar to Micro Air Vehicles (MAVs), MAV designers have looked to mimic features of biological flyers in an attempt to improve their aerodynamics [8]. One objective of the study is to develop a better understand of how the membrane and flow interact.

MAVs are classified as an aircraft with a wing span of 6 inches (15 cm) or less and tends to operate at airspeeds of 15 m/s or less [8], [9]. With the advancement of technology, MAVs are now relatively easy to deploy and can have endurance times of 20-60 minutes depending on its application. Payload packages are small enough allowing sophisticated controls, visual imagery, and/or task specific sensors to be mounted on them. While MAVs may seem tailored to military applications the civilian sector can also benefit from current advances such as aiding in the following: search and rescue, wildfire monitoring, and agricultural development [9]. While MAVs have been in existence for the past few decades, recent bio-inspired MAVs started utilizing

lightweight flexible lifting surfaces in an effort to mimic biological flyers, to help aid in their performance.

One of the main challenges with MAV design is the significant drop in aerodynamic performance associated with flight in the low Reynolds number regime. In low Reynolds number flight, parameters such as adverse pressure gradient, surface roughness, airfoil's leading edge shape, and free stream turbulence intensity may cause the flow to separate at the airfoil's leading edge. Depending on if the flow transitions to a turbulent flow, it may entrain enough high momentum fluid to reattach itself forming a separation bubble [10] typically adding some unsteady features. Unlike flight in a high Reynolds number flow, flight in low Reynolds number first experiences a separation bubble at the leading edge where the bubble then grows longer until it reaches the trailing edge [11]. Airfoils with long separation bubbles change the pressure distribution yielding a significant drop in lift and an increase in drag [12]. In the act of bubble bursting, meaning the free shear layer is no longer attached, the wing may experience a undesirable change in pitching moment [12]. This investigation will look at the interactions between the fluid and structure of low aspect ratio wings in a low Reynolds number flow. A further understanding of this process would benefit the MAV community as well as other applications that incorporate the use of compliant membranes such as: sail boats, hang gliders, and power kites [13]–[15].

## **Background**

### **Previous Investigations**

The University of Florida was one of the first to adopt a flexible membrane wing within their MAV design [16]. Early investigations by Ifju et al. [8] compared a MAV with a rigid wing to various MAVs with a batten reinforced membrane wing. While different

batten configurations were examined, results concluded with the membrane MAVs requiring less user input to maintain a stable flight. Wind tunnel tests also showed the membrane MAVs obtaining a higher lift coefficient and a delay in stall when compared to a rigid wing MAV.

Later Stanford, Ifju, Albertani, and Shyy [17] investigated the effects between a Batten-Reinforced (BR) MAV, to a Perimeter-Reinforced (PR) MAV. A BR wing utilizes a rigid leading edge with battens (thin strips of material/ribs) extending from it. The membrane is attached to the battens allowing it to have a free trailing edge, Figure 1-1B. A PR-wing is a rigid wing with an enclosed section removed. A membrane is then used to cover over the hollow section, while being secured by its perimeter, Figure 1-1A. Results led to a few different trends at low AOAs, the membrane on the BR-MAV would oscillate thus changing its camber resulting in lift. However, the free trailing edge would deflect upward resulting in a nose down movement thus effectively cancelling each other. The PR-MAV had a large increase in lift from the bellowing of the membrane, this was accompanied by an increase in drag. Since the PR-MAV membranes were allowed to move in 2D, the interactions of the wing tip vortices could possibly create a rolling instability, however a further investigation was needed to confirm.

Rojratsirikul et al. [18], [19] investigated the Fluid Structure Interactions (FSIs) of a 2D latex rubber membrane airfoil with a rigid leading edge and trailing edge. Early investigations utilized timed resolved PIV to capture the 2D flow-field velocities while laser reflections off of the membrane's surface captured the membrane's fluctuations and vibrational modes. A hot wire was also used to examine the spectral characteristics of near wake shedding. Results led to a strong coupling of membrane oscillations to

shear layer height with an increase in vibrational modes with increasing freestream velocity. There also exists a possible coupling between the vortex shedding and membrane fluctuations. The FSIs were again examined for a 2D latex rubber membrane airfoil with a rigid leading edge and trailing edge however, different models of pre-tension and excess length were used. Results concluded, pre-tensioned membranes had similar traits of rigid airfoils whereas membranes with excess length had a reduction of separated flow and an increase in the number of vibrational modes.

Rojratsirikul et al. [20] continued their investigations this time of a finite perimeter reinforced membrane model, in which three-dimensional (3D) effects could be analyzed. Again, membrane fluctuations, membrane modes, 2D flow-field velocities, and near wake shedding were investigated. Their experimental set-up remained relatively similar to previous investigations however, membrane vibrations and modes were captured independently by DIC. They showed the trends of the finite PR wing closely resembled that of the solid leading and trailing edge wing. The finite PR membrane wing showed a strong coupling between the vortex shedding and membrane fluctuations in the post stall region similar to that of their larger aspect ratio case.

Visbal et al. [21] conducted a numerical simulation to capture the FSIs obtained experimentally by Rojratsirikul et al. [18]. They utilized a 6<sup>th</sup> order implicit large eddy simulation for the fluid dynamic solver coupled with a nonlinear finite element for the membrane structural solver. The AoA for the simulated data was set to 14° to match that of the experimental data. When the appropriate grid spacing was selected the numerical results qualitatively agreed with the experimental results. Numerical simulations were able to capture a close coupling between the membrane fluctuations

and unsteady flow over the membrane as well as vortex roll up occurring at the trailing edge.

Aerodynamic forces and flow-field fluctuations were measured on thin slightly cambered BR membrane wings. Hu et al. [22] varied the membrane's cell aspect ratio by either increasing or decreasing the number of battens within the wing. This change in batten spacing was done to examine the effects of membrane flexibility. They concluded the BR membrane wings had improved aerodynamic performance when compared to its flat plate counterpart. Shown from PIV measurements, the membrane wings had the ability to reduce the amount of separated flow by automatically adjusting its camber to adapt to the pressure differences. When testing the different BR membrane wings it became apparent that wing flexibility (batten spacing) was important. The highly flexible membrane wings would experience a trailing edge flutter which would result in a decrease in lift and an increase in drag.

Numerical simulations were performed by Smith and Shyy [23], utilizing the Reynolds averaged Navier-Stokes equation as the fluid dynamic model while employing the shear stress transport model to handle the closure problem. Young-Laplace equation, a 2D elastic membrane equation, was implemented to govern the structural dynamics. The model was then compared to experimental data taken by Greenhalgh et al. [24], Sugimoto et al. [25], and Newman et al. [26]. Results for coefficient of lift were within 5% of agreement at low AoA and for the lower Reynolds number ( $10^5$ ) experimental data. However, large deviations were experienced at high AoAs and larger Reynolds numbers. Differences in Reynolds number, membrane support, and wall

effects within the experiments were some thoughts on what may have contributed to the discrepancies [23].

To help compare with other flexible membrane investigations an aeroelastic Pi parameter was created by Smith and Shyy [27], where  $\pi_1$  and  $\pi_2$  are defined in Equations 1-1 and 1-2 respectively. E is the Young's modulus of the membrane, t is the membrane's thickness, b' is the membrane's cell span,  $^{\circ}S$  represents the membrane's pre-stress which is related to the pre-strain within the membrane by the modulus of elasticity  $E\varepsilon$ , and q is the dynamic pressure at freestream conditions. These two nondimensional parameters relate the membrane's stiffness (Et) to the aerodynamic load (qb'). The  $\pi_1$  parameter is used for un-tensioned membranes while the  $\pi_2$  parameter is used for pre-tensioned membranes [27].

$$\pi_1 = \left( \frac{Et}{q_{\infty} b'} \right)^{\frac{1}{3}} \quad 1-1$$

$$\pi_2 = \left( \frac{{}^{\circ}St}{q_{\infty} b'} \right) \quad 1-2$$

A further investigation into the aeroelastic response of BR membrane wings was conducted by Johnston et al. [28]. Wing configurations consisted of thin flat frames with varying batten spacing and membrane pre-tension. Results obtained from video imagery showed after an onset velocity the membranes would flutter resulting in what Johnston et al. describes as Limit Cycle Oscillations (LCOs). An increase in both membrane pre-tension and number of battens would result in an increase in onset velocity. It was also found that after certain velocities and AoAs the magnitude of the LCOs would start to decrease [28], [29].

## Predecessor Investigations

The collaborations between the University of Florida and the University of Alabama built the foundation which this study is based off of. In 2008, Mastramico and Hubner [30] started investigating the wake characteristic of a solid plate compared to that of different membrane models, PR, BR and BR scalloped, by means of hot-wire anemometry. Results concluded with the BR scalloped membrane producing a consistent reduction in the local profile drag coefficient when compared to the solid plate, PR and BR models. The BR scalloped membrane also produced a smaller but wider wake deficit when compared to the other models. To further understand the effects of membrane geometry, Hicks and Hubner [31] conducted a parametric study. Load data and hot-wire anemometry was taken on BR membranes with varying cell depth, batten spacing, and trailing edge scalloped depth. Their findings led to trends such as scalloping the trailing edge of membranes decreased both the lift and the drag. However, scalloping had a greater effect on the drag thus improving the overall aerodynamic efficiency. Another trend was while scalloping had a slight decrease in lift an increase in the cell geometry, the membrane's chord and span size, led to a large increase in lift. A BR membrane wing with a cell aspect ratio of 1 and a 25 percent scalloped (with respect to the chord) trailing edge resulted in being the most aerodynamically efficient.

To that point, all investigation consisted of a membrane model composed out of latex rubber with zero pre-tensioning. Working with the latex rubber material provided a few challenges, models degraded within a week's time. Also, applying a consistent and repeatable pre-tension in the membrane was nearly impossible. These challenges led into an investigation comparing the flow response and membrane vibrations to changes

in membrane material properties. Scott et al. [32] examined the membrane oscillations and flow-field fluctuations of both a latex rubber membrane and a silicone rubber membrane. Synchronized hot-wire anemometry and laser vibrometry allowed correlations to be obtained between the membrane's oscillations and the flow-field fluctuations. At velocities below the membrane's onset velocity, membrane's flutter was not visually present, which resulted in a low coherence between the FSIs. At these pre-onset velocities, the membranes would vibrate at their respective natural frequencies. However after the membrane would start its LCOs, a large coherence ( $>0.5$ ) was present. While the latex and silicone rubbers had slightly different frequencies at both pre-onset velocity and during its LCOs, both materials exhibited the same trends. Abudaram et al. [33] investigated in a method to accurately obtain a desired pre-tension within a membrane. Their investigation used a silicone rubber material, where the silicone rubber was heated and attached to a frame, the strain was then measured by DIC. The results concluded with the silicone rubber obtaining a linear strain vs. temperature curve. With this relationship for the silicone rubber, new flexible membrane wing models with specific pre-tension were created and later investigated by Timpe et al. [34], [35]. Their models had a high aspect ratio (4.3) multi-celled silicone rubber membrane in a BR wing with a scalloped trailing edge. Timpe et al. investigated the FSIs by synchronized time-resolved PIV and DIC. Results showed the membrane wings had a reduction in both the shear layer height and wake deficit compared to its flat plate counterpart. Furthermore, a strong coupling existed between the membrane's frequency and the dominate flow-field frequency. When the membrane's characteristics were changed by AoA and/or tension, so did its corresponding flow-field. At a parallel time,

Zhang et al. [36] studied the lift characteristics of the same membrane models as Timpe et al. Results showed the high aspect ratio, scalloped trailing edge membranes when compared to its flat plate counterpart had an improved aerodynamic efficiency.

### **Current Investigations**

The present study is aimed at gaining further knowledge into the fluid and structure interactions of low aspect ratio compliant membrane wings in a low Reynolds number flow. Characteristics of the streamwise flow-field and 3D membrane surface deformations are acquired by synchronizing a time-resolved PIV system and DIC system. The analysis will include the structural dynamics of both the membrane oscillations and the unsteady flow-field measurements. A flat plate model will be used as a baseline case in which the membrane models flow-field can be compare with. Additionally, the motion in which the membrane travels in will be analyzed and an attempt will be made to describe the standing wave and traveling wave coupling. Finally, correlations between the membrane's oscillations and flow-field will be examined.

The remainder of this thesis will be structured as follows. Chapter 2 will describe the experimental set-up including the facilities, equipment, models and processing techniques. This will be followed by the results and discussion of the flow-field and membrane surface deformations in Chapter 3. Finally, Chapter 4 will bring some conclusions about the fluid and structure interactions followed by a brief discussion on further investigations.



Figure 1-1. Flexible membrane MAVs. A) PR MAVs. B) BR MAVs (source [17])

## CHAPTER 2 FACILITIES AND EXPERIMENTAL SETUP

This chapter is laid out as follows, an overview of the two different testing facilities will be provided. Next, the wing geometry and the steps involved in creating the membrane wings will be discussed. Then, a detailed description of the equipment used to acquire data will be given. This will be followed by a description of the experiments conducted along with the experimental setup. Finally, the pre and post processing techniques used will be discussed.

### **Facilities**

The experiments performed within this investigation were conducted in two different facilities. The first experiments were conducted at the University of Florida's Research and Engineering Education Facility (REEF) using the Aerodynamic Characterization Facility (ACF). The second set of experiments were performed at the University of Florida's main campus using the Engineering Laboratory Design Wind Tunnel (ELD-WT).

### **Aerodynamic Characterization Facility**

The ACF is an open jet, open return wind tunnel specifically designed for experiments in the low Reynolds number regime. A photograph of the facility is included in Figure [2-1A](#). Flow enters the facility where it passes through a 3.05 m square bell mouth entrance before it goes through a conditioning region. The conditioning region consists of a metal honeycomb and several screens followed by a constant area settling region. After the 1.4 meter long settling region the flow undergoes an 8 to 1 area ratio contraction. Finally, after the contraction, the flow exits the inlet of the open jet test section with dimensions of 1.07 m by 1.07 m. Downstream of the inlet (3.05 m) lies the

diffuser which houses an inline 50 Hp axial blower with a variable frequency drive. Experiments conducted using hot-wire anemometer in the ACF yielded a turbulence intensity ( $|u'|/u$ ) of 0.16% at a freestream velocity of 10 m/s, which is the velocity utilized for all experiments conducted in this study. More details describing the ACF and flow quality can be found in Albertani et al. [37].

### **Engineering Laboratory Design Wind Tunnel**

The ELD-WT is a low turbulence closed loop, recirculating facility and is displayed in Figure 2-1B. The air is moved through the tunnel by an inline 200 Hp axial blower with variable frequency drive. Turning veins are used at each intersection to help direct the flow around the bends. Air enters the conditioning region where it passes through an aluminum honeycomb and several anti-turbulence screens. Next, the air then goes through a 25 to 4 area ratio contraction where it finally enters the test section at a cross-sectional area of 0.61 m by 0.61 m (24 in by 24 in). Using hot-wire anemometer the ELD-WT yielded a turbulence intensity ( $|u'|/u$ ) of 0.1% at a freestream velocity of 10 m/s. More details describing the ELD-WT and flow quality can be found in Sytsma [38].

### **Models**

Throughout all experiments three models were investigated, two different membrane wing models and a rigid flat plate, where the rigid plate model was only used during PIV experiments. All of the models had an aspect ratio (span/chord length) equal to 2 with a rectangular outer dimension of 152.4 mm by 76.2 mm (6 in by 3 in). Each model was constructed out of 7075-T6 aluminum and had a thickness of 0.8 mm. The membrane wings had cut-outs in the aluminum where flexible material was utilized to fill-in the structure creating the batten reinforced wing geometry. Two different

membrane wings were tested, the first membrane wing had a 1 percent pre-tensioned membrane while the second membrane wing had a 4 percent pre-tensioned membrane. As mentioned in the introduction, the membrane wings utilized in this study were constructed out of silicone rubber due to its advantages over latex rubber in terms of the life span. The process that Abudaram et al. [33] developed was used to obtain a desired pre-tension within the membrane. The silicone rubber is first heated and cooled down several times via a hot plate to prevent hysteresis effects. When heated, the silicone rubber undergoes an isotropic expansion. Thus, when adhered to the metal frame and allowed time for cooling, a measurable strain is present within the membrane. Figure 2-2 shows the linear relationship between the temperature of creation and measured pre-strain within the silicone. Figure 2-3 shows the pre-strain within the membrane at creation while Table 2-1 provides the membrane model's properties. The BR frames consisted of three symmetric membrane cells, each membrane's trailing edge was scalloped 25 percent (with respect to the chord) as Hubner et al. [31] found this to be the most aerodynamically efficient configuration. Models used during testing can be seen in Figure 2-4, while nomenclature and geometric representation of the membrane model is provided in Figure 2-5. Table 2-2 list the geometric dimensions of the membrane models.

### **Experimental Equipment**

Two different non-intrusive measurement techniques were implemented within this investigation to measure both the velocity field and the membrane motions. The flow-field was measured by PIV and the membrane surface deformations were measured by DIC. Both systems were synchronized together where each PIV snap shot would trigger the DIC system.

## Particle Image Velocimetry

Two components of velocity (U and V) were acquired using a “Time Resolved” PIV system from Dantec Dynamics. This system consisted of a series 800 double-cavity ND:YAG (Lee Laser) and two Integrated Design Tools XS-5 high-speed CMOS cameras equipped with Nikon 105 mm lens set to an f-number equal to 2.8. Timing and acquisition were controlled with Dantec Dynamic’s Dynamic Studio V3.31 software [39].

During synchronized testing, the sampling rate was set to 800 Hz, this was the max sampling rate based on the PIV cameras at selected resolution. It was previously found that the membranes tend to oscillate between 50-90 Hz, meaning a sampling rate of 800 Hz would provide adequate time resolved data [34]. Since images are stored on board the cameras limited memory, the cameras original resolution of 1280 pixels by 1040 pixels was decrease to 1280 pixels by 600 pixels. This reduction in pixels was done to obtain more images at the desired sampling rate. Assuming a normal distribution, the PIV data was within the 95 percent confidence interval by the 300<sup>th</sup> sample. Figure 2-6 shows the statistical convergences for the PIV data with the 1 percent pre-tension membrane model at 16° AoA. Uncertainty within the PIV data was found to be 5.6 percent of the freestream condition, further information on PIV uncertainty can be found in APPENDIX A.

Two high speed PIV cameras were used to capture the flow above the models and within the near wake region. The first camera, the model camera, had a field of view of 85.35 mm by 40.01 mm which resulted in a 15 pixels/mm calibration. The second camera, the wake camera, had a field of view of 116.3 mm by 54.53 mm, which resulted in an 11 pixel/mm calibration. The cameras were arranged so there was an overlapping section between each camera, this region had a size of 6.35 mm. Figure 2-

7 shows the model camera and wake camera fields of view along with the overlapping region. Vector fields were computed using an adaptive correlation method. Before this process was done, a mean background was subtracted from each image set. The background subtraction helped reduce the noise the cameras sensor experienced. A four step iterative process with an adaptive-window cross-correlation algorithm was applied to each data set [39]. An initial interrogation area (IA) of 128 pixels by 128 pixels with a 25 percent overlap was applied. Each pass reduced the IA size until the final 16 pixel by 16 pixel IA size was achieved. The vector fields were then imported into MATLAB® for further processing.

### **Digital Image Correlation**

The 3D membrane surface deformations were measured using a high speed Correlated Solutions DIC system. This system utilizes two Vision Research high-speed Phantom V7.1 SR-CMOS cameras equipped with Tamron AF 28-300 mm aspherical lens set to an f-number equal to 7.8. The cameras were controlled using Phantom cameras 675.2 control software and the deformations were obtained using Correlated Solutions VIC-3D 2010 software [40]. To help provide uniform lighting a 250 watt halogen lamp was shined on the membranes speckled pattern.

During synchronized tests the sampling rate of the DIC system was matched to that of the PIV system, 800 Hz. Later independent DIC tests also sampled data at 800 Hz in order to keep consistent within the different experiments. DIC works by comparing the random speckled pattern on an area of investigation when no loads are applied to that of the same area as it travels through its motions. VIC-3D applies a gray scale cross-correlation method to each subset to obtain the deformations. To obtain a random speckled pattern on the membranes, a light mist of paint from an aerosol can that had a

modified tip was applied. This was found to create speckles of paint random enough to be processed, speckles can be seen in Figure 2-4. The subset size was selected to be 19 pixels by 19 pixels with a step size of 3. This resulted in a grid spacing of 0.57 mm in both the x and z directions (streamwise and spanwise directions). A Gaussian weight was applied to the subset such that the center was weighted. To better achieve sub-pixel accuracy an optimized eight coefficient interpolation filter was applied. A normalized squared difference correlation-criterion was selected specifically for its ability to be unaffected by scale in lighting [40]. The coordinate system which displacement values originate from is based off the reference image. The origin is located at the mass centroid of all measured points within the reference image. The Y-axis (vertical axis, axis where displacement values are located) is normal to the best-fit plane within the reference image. After displacement values were obtained they were imported into MATLAB<sup>®</sup> for additional post processing.

### **Synchronization**

To synchronize the PIV system with the DIC system posed a unique challenge. The DIC cameras needed a 5 volt signal for an external trigger and the PIV cameras produced a 3 volt pulse on its sync out port. This 3 volt pulse conveniently was only produced on the first frame of each image pair. The pulse was sent to a Tektronix type 114 Pulse Generator where it reshaped the signal to a 5 volt square wave with negligible time delay. Due to the set-up, with the PIV laser firing in the direction of the DIC cameras, HOYAs multi-coated high pass optical filters were placed over the lens. These filters are designed to block light with a wavelength  $< 600$  nm thus not allowing any of the lasers 532 nm light to shine through.

## Experimental Description

The data presented within the study was collected in two different data sets. The first data set consisted of synchronized PIV and DIC in order to understand the interactions between the flow and the membrane. While the second data set consisted of independent DIC measurements to get a more detailed understanding of the membrane's motions.

### Synchronized PIV and DIC

Synchronized PIV and DIC experiments were conducted in the ACF at 10 m/s. The Reynolds number, Equation 2-1, based on freestream velocity and model's chord length was calculated as 50,500 ( $\approx 50,000$ ), this value was kept fixed throughout all tests. Figure 2-9A shows the experimental set-up where the PIV and DIC measurements were synchronized. This set-up was such that the PIV laser probe was positioned beneath the model. Due to the limited length of the laser probe the models needed to be inverted. Since the models were inverted and positioned in the center of the ACF's inlet, the DIC cameras were placed above the inlet and out of the flow. The DIC cameras were adjusted so the field of view obtained was the speckled pattern of all three membrane cells (the speckled pattern was applied to the underside of the membrane models). The PIV cameras were positioned on the side of the inlet normal to the model's span. The first camera (model camera) focused on the leeside flow of the models while the second camera (wake camera) focused on the area directly downstream of the models. Synchronized data was taken on two models, the 1 percent pre-tension membrane wing, and 4 percent pre-tension membrane wing. Independent PIV data was taken on the flat plate wing so there would be a baseline case for comparison of the membrane wings. A collection of 1044 synchronized images of PIV

and DIC data were acquired for all models at a range of AoAs (4°, 8°, 12°, 16°, and 20°). Again only PIV data was taken on the flat plate case. A digital inclinometer was used to manually set the models AoA to ± 0.2°, Figure 2-8.

$$Re_c = \frac{\rho_f U_\infty c}{\mu} \quad 2-1$$

### **Independent DIC**

Further investigation into the membrane's motion was conducted in the ELD-WT. These experiments were to supplement the synchronized data previously taken. Models and air speed during these experiments remained the same as previous, a 1 percent pre-tension membrane model and a 4 percent pre-tension membrane model were tested at 10 m/s. Tests consisted of independent DIC experiments at a range of AoAs of 4°, 8°, 12°, 16°, 20°, 24°, 28°, and 32°. Since this was the first time these experiments were conducted in the ELD-WT, a new mounting arm needed to be created. To insure the mounting arm and wind tunnel did not influence the membrane's motions, vibration tests were taken on both the mounting arm and the wind tunnel, for further information see [APPENDIX B](#).

Even though PIV data was not taken, the models were still inverted to match previous experiments. The DIC cameras and lamp were positioned above the test section such that all three membrane cells fit into the cameras field of view. Again, the membrane wings were supported as they were in the previous experiment, two thin symmetric airfoil hangers attached to the outer portion of the wings. The hangers were then attached to a circular rod, experimental set-up can be seen in Figure 2-9B. To further analyze the influence of the wing tip vortices, the model's mounting hardware was changed to a single airfoil hanger supporting the center of the membrane's frame.

Experiments were repeated at AoAs of 8°, 16°, and 24° while being supported only by the center mount. Figure 2-10 shows the membrane wing being supported by the single airfoil hanger.

### **Post-Processing**

The flow-field fluctuations and membrane oscillations were further analyzed by calculating the statistical mean and Root Mean Square (RMS) values. Additional calculation consisted of obtaining Power Spectral Densities (PSD) and cross correlations of the time dependent data. Extra operations involved applying a dynamic mask to the PIV vectors as well as an outlier detection. All post-processing operations were done in MATLAB® R2010b.

### **PIV**

The PIV vectors (both U and V components) were imported into MATLAB® where a dynamic mask was applied to each time frame. The dynamic masks were used to remove data where the outer membrane would cast a shadow covering the center membrane (where PIV data was taken at). Additionally, a mask was applied to each time frame when the center membrane extended past the chord line into the flow-field. After the masks were applied, a Multivariate Outlier Detection (MVOD) was implemented to eliminate any spurious vectors. MVOD is a non-spatial dependent operation that looks at the vector fields as a whole. A multivariate projection is calculated for each data point where all projections are compared to a scalar threshold, further information can be found in Griffin et al. [41]. The MVOD would typically eliminate 5 percent or less spurious vectors, however since over 1000 vectors were acquired the statistics of mean flow properties were determined to still converge.

## DIC and PIV

Ensemble averages of the velocity field and membrane displacements were used due to the fact they were found to be stationary in time at a given spatial location. Each ensemble was separated by its mean and fluctuating component based on classical Reynolds decomposition, Equation 2-2. The mean and RMS fluctuations were calculated by Equations 2-3 and 2-4 provide by Bendat and Piersol [42].

$$\tilde{X} = X_{mean} + X' \quad 2-2$$

$$X_{mean} = \langle \tilde{X} \rangle = \frac{1}{N} \sum_{i=1}^N \tilde{X}_i \quad 2-3$$

$$X_{RMS} = \sqrt{\frac{1}{N-1} \sum_{i=1}^N X_i'^2} \quad 2-4$$

The dominant frequency of both the membrane's oscillations and velocity field's fluctuations were obtained by a Discrete Fourier Transform (DFT) to compute spectra. Equation 2-5 shows the Fourier transform at discrete frequencies. Equation 2-6 is used to calculate the frequency resolution within the data, where N is the record length and  $F_s$  is the sampling frequency. Only one record of length 1044 was used in the synchronized data resulting in a frequency resolution of 0.77 Hz. The independent DIC data was broken into a record length of 586 and averaged over 5 blocks, which resulted in a bin width of 1.37 Hz. In the end, Equation 2-7 was used to compute the one sided Power Spectra Density (PSD). This equation used Welch's method while implementing a rectangular window with 50 percent overlap. Additionally, a correlation analysis was also computed on the independent DIC data. Equation 2-8 was used to compute the correlation between the membrane fluctuations at one specific location X, with the

membrane fluctuations at a different spatial location  $Y$ . The cross correlation is normalized so the value of the autocorrelation computed at  $t=0$  is equal to one.

$$X(f_k) = X_k \Delta t = \Delta t \sum_{n=0}^{N-1} x_n \exp \left[ \frac{-j2\pi kn}{N} \right] \quad \text{where } k = 0, 1, 2, \dots, N - 1 \quad 2-5$$

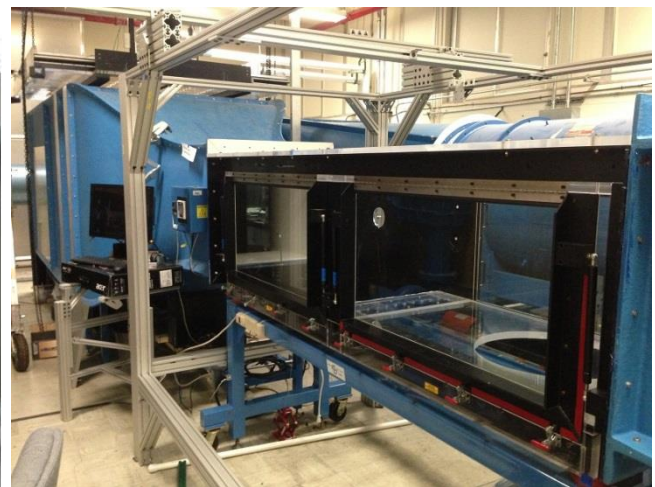
$$\Delta f = \frac{f_s}{N} \quad 2-6$$

$$G_{xx}(f) = \frac{2}{\Delta f * N^2} E[X^* * X] \quad 2-7$$

$$C_{xy}(\tau) = \frac{E[X' * Y']}{(\sigma_{x'} \sigma_{y'})} \quad 2-8$$



A



B

Figure 2-1. Low speed test facilities. A) ACF located at REEF (source [37]). B) ELD-WT located at UF's main campus. Photo courtesy of author.

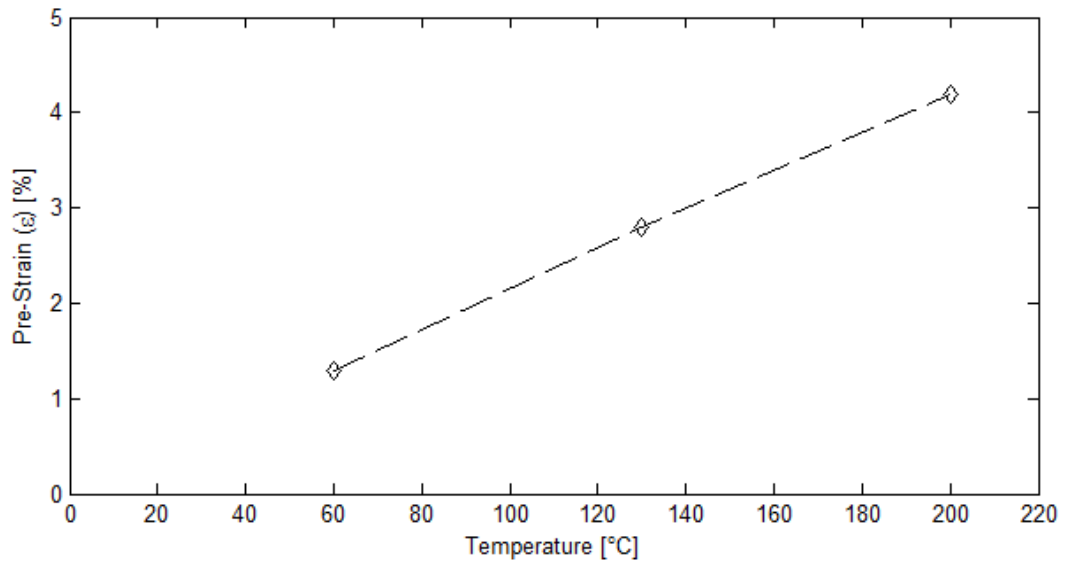


Figure 2-2. Linear relation between temperature of creation and measured pre-strain.

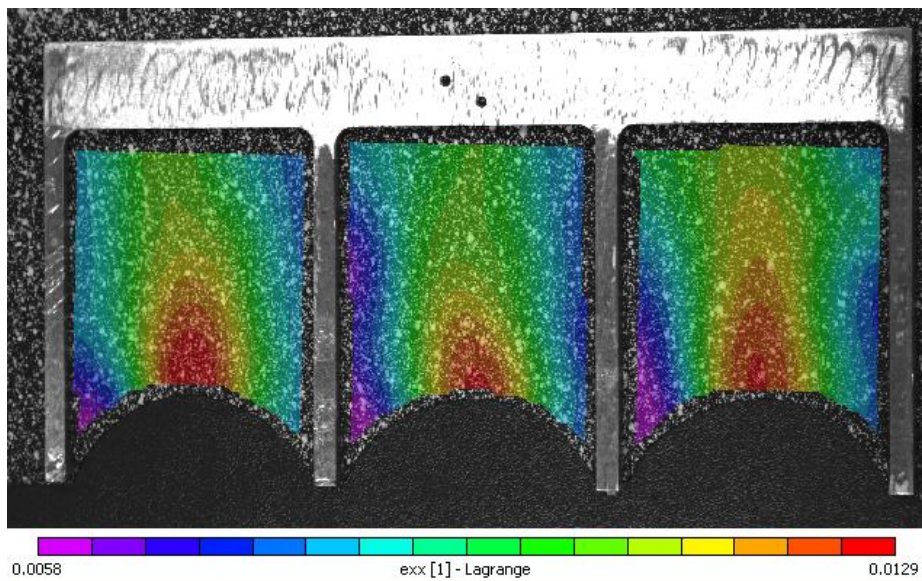


Figure 2-3. Measured pre-strain within the membranes.

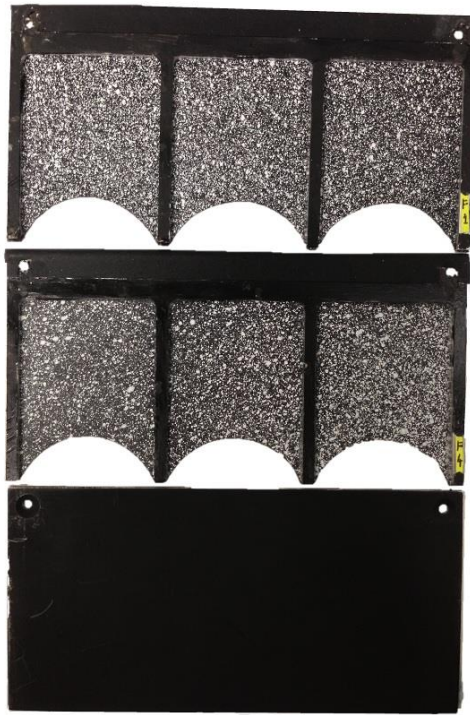


Figure 2-4. Aspect ratio 2 membrane models and flat plate model. Photo courtesy of author.

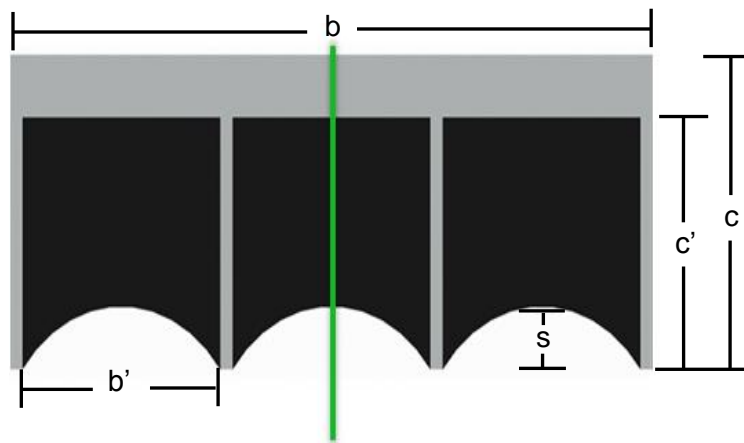


Figure 2-5. Membrane wing nomenclature. Green line represents plane where PIV data was taken at.

Table 2-1. Membrane's properties.

Models Average Spanwise Pre-Strain [%]± 0.1	Temperature of Creation [°C]	$\Pi_2$	Membrane Thickness [mm]	Silicone Rubber Elastic Modulus [Kpa]
1.0	45	0.36	0.34	385
4.0	190	1.43		

Table 2-2. BR membrane model dimensions. All values are in units of mm.

Span, b	Cell Span, b'	Chord, c	Cell Chord, c'	Aspect Ratio	Scallop Depth, s	Batten Width	Frame Thickness
152.4	45.7	76.2	61	2	15.2	3.82	2.8

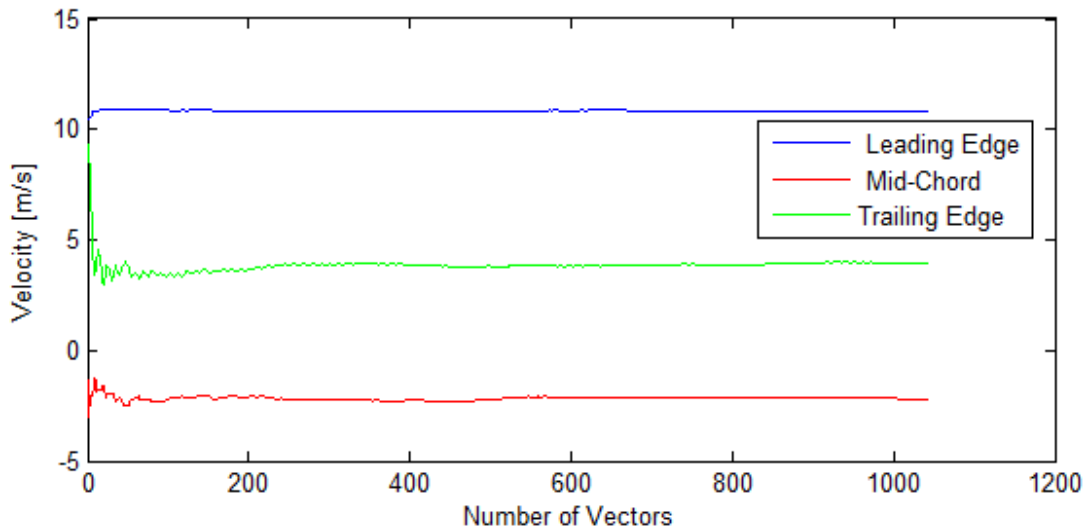


Figure 2-6. Statistical convergences for the 1 percent pre-tension membrane model at 16° AoA.

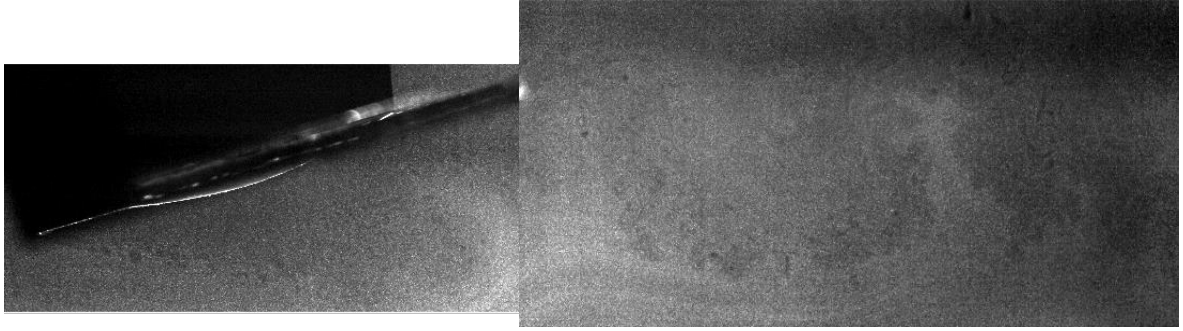


Figure 2-7. Combined fields of view from PIV cameras.



Figure 2-8. Digital inclinometer on top of model. Photo courtesy of author.

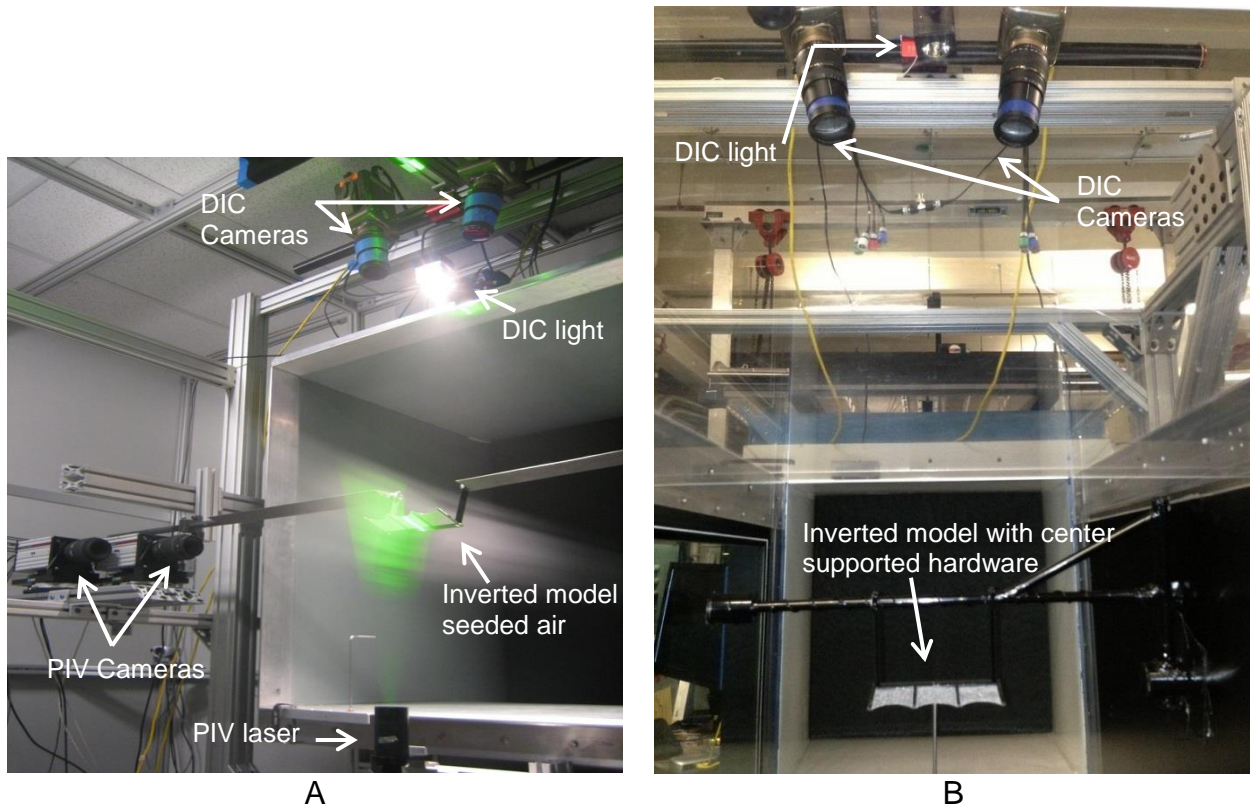


Figure 2-9. Experimental set-up. A) Synchronized experimental set-up within the ACF. B) Independent DIC set-up within the ELD-WT. Photos courtesy of author.

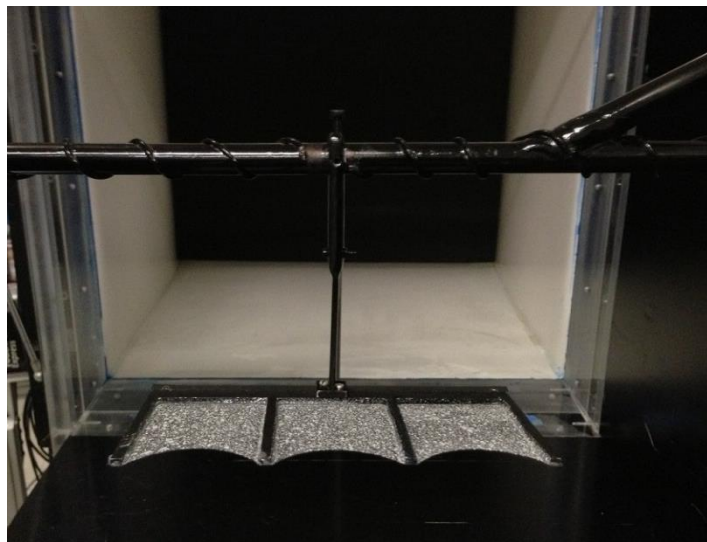


Figure 2-10. Membrane model with center supported hardware positioned within the ELD-WT. Photo courtesy of author.

## CHAPTER 3 RESULTS AND DISCUSSION

This chapter will present and discuss the results obtained for the fluid structure interactions of a low aspect ratio, passively compliant, BR membrane wing in a low Reynolds number flow. The results will be discussed in the following manner; first, the flow-field measurements obtained from 2-component PIV will be examined. This will be followed by the membrane's surface deflections measured by DIC. Finally, correlations between the flow-field and membrane oscillations will be provided.

### **Flow-Field Measurements**

The 2-component (U-component and V-component) flow-field measurements were acquired using the time resolved PIV system discussed in the previous chapter. The flow above a flat plate model, and in its near wake region, provided a baseline case to compare the effects of the membranes. This baseline case was used to compare both the 1 percent pre-tension and 4 percent pre-tension membrane models. In all the plots presented here all length scales and velocity scales have been normalized by the full chord length (76.2 mm) and freestream velocity (10 m/s). PIV data was obtained in the streamwise direction along the center of the middle cell for the membrane models, and also in the center of the flat plate model. Data was recorded on each model at five different AoAs, 4°, 8°, 12°, 16°, and 20°. The analysis includes both mean and turbulent time averaged velocity fields to highlight different aspects within the flow-field. First, the time averaged U-component ( $\langle U \rangle$ , U-mean) can be seen in Figure 3-1. The color scale for these plots has been chosen such that regions of dark blue represents reverse flow ( $U < 0$ ). This is followed by  $U_{RMS} = \sqrt{\langle u'^2 \rangle}$  in Figure 3-2. The third time averaged quantity evaluates the Reynolds Shear Stress (RSS) term. Equation 3-1 shows the Reynolds

Averaged Navier-Stokes equation obtained from Pope [43], where the last term  $-\rho\langle u'v' \rangle$  is the RSS term. Keeping note of the negative sign in front of the RSS term, when both  $u'$  and  $v'$  are of the same sign, on average, the RSS will be a negative value. However, when both  $u'$  and  $v'$  are of the opposite signs, on average, the RSS will be a positive value, Figure 3-3. For all of these figures the flat plate cases (column A) have a solid wing geometry frame superimposed on the PIV plots to help visualize the flow. The membrane models (columns B and C) have a 20 percent solid leading edge frame geometry while the remaining 80 percent of the frame is represented by dashed lines to denote the battens. Also within the figures, one cycle of membrane oscillations obtained from DIC have been superimposed to further help visualize the flow dynamics.

$$\rho \frac{\overline{D}\langle U_j \rangle}{\overline{D}t} = \frac{\partial}{\partial x_i} \left[ \mu \left( \frac{\partial \langle U_i \rangle}{\partial x_j} + \frac{\partial \langle U_j \rangle}{\partial x_i} \right) - \langle p \rangle \delta_{ij} - \rho \langle u'_i u'_j \rangle \right] \quad 3-1$$

Examining the flat plate model, the evolution of the streamwise velocity component for the flow-field is shown in Figure 3-1. At 4° AoA the flow slightly increases in amplitude over the leading edge and appears to remain attached as it traverses down the wing. As the AoA is increased, the flow still remains attached however there is a noticeable decrease in velocity near the surface. Comparing the flat plate model to its larger aspect ratio counterpart investigated by Timpe et al. [34], the lower aspect ratio wing experiences a delay in AoA before the flow becomes stalled. For this wing, stall sets between 8 and 12 degrees while for the larger aspect ratio wing this happens at angles of slightly less than 8°. The same delay in stall was also seen in Zhang et al. [36] were they measured force data on both low and high aspect ratio flat plate models. This delay is consider to be the effects attributed to the stronger influence the wing tip vortices have on the flow surrounding the model. Torres and Mueller [44] proposed as

the aspect ratio decreases the effects of wing tip vortices become stronger. The stronger vortices energized the flow above the wing's surface thus delaying the onset of separated flow [44], [45]. It is not until 12° AoA does the flow above the flat plate model experience reverse flow. The flow at 12° no longer has enough momentum to remain attached, thus separating and creating a separation bubble. Due to the size of the separation bubble, reverse flow is now present within the near wake of the model resulting in a significant increase in wake deficit. Using a steady control volume approach, the near wake momentum deficit can be proportionally related to drag, hence an increase in wake deficit is an indication of an increase in drag [46]. As the flat plate is increased to a higher AoAs an increase in the shear layer height, amount of reverse flow, and wake deficit were all observed. Finally at the last angle recorded, 20° AoA, the flat plate experienced a massive separated region above the surface as well as a large amount of reverse flow in the near wake, creating a massive wake deficit.

The flow-field for the 4 percent pre-tension membrane model and 1 percent pre-tension membrane model, Figure 3-1 - Figure 3-3 columns B and C respectively, will be compared to the baseline flat plate case. When examining the plots there are a few trends that initially stand out. One of the first trends to note is the reduction in shear layer height. Examining the U-RMS fluctuations in Figure 3-2 this reduction can be seen throughout all AoAs tested. The membrane's compliant feature is seen to help pull the shear layer closer to the membrane's surface. As the shear layer remains closer to the membrane's surface an increase in the amplitude of the streamwise flow at the leading edge is noted. The membrane models demonstrated accelerated flow at the leading edge of approximately 15 percent greater than the flat plate case. Another trend to note

is the significant decrease in reverse flow above the model's surface and in the near wake. Comparing with the flat plate model at 12° AoA where a large separation bubble was present, the flow over the membrane models have a relatively small separation bubble closer to the leading edge. Increasing the AoA further highlights the reduction in both the amount of reverse flow as well as the amount of turbulent flow in the near wake the membrane models produce compared to the flat plate model. Part of the reduction in reverse flow can be attributed to the membrane models being able to change their camber in the presence of a pressure difference. The increase in camber effectively allows the flow to reattach whereas in the flat plate case the flow remains separated. Examining the near wake leads to another trend, the membrane models have a major decrease in peak wake deficit velocities. At lower AoAs, the membrane models have a smaller but wider wake deficit. However at higher AoAs, a narrowing of the wake and a substantial decrease in deficit is experienced.

Looking at both the RSS and instantaneous vorticity generated by the membrane models leads to some insight on how the membrane motions help aid in the reduction of reverse flow present in the near wake, Figure 3-3 and Figure 3-4 respectively. Examining the RSS obtained for the flat plate cases, momentum transfer of positive sign (opposite sign deviations) is seen within the shear layer. While momentum transfer of negative sign (same sign deviations) is seen beginning at the leading edge and trailing edge. As AoA is increased RSS continues to grow. Membrane models share similar features at low AoA with positive RSS seen in the shear layer as well as negative RSS seen at the leading edge and trailing edge. At higher AoAs ( $\alpha > 8$ ) the membrane's influences becomes apparent. The membrane models have a slight reduction in positive

RSS (lower momentum fluid) within the shear layer while the negative RSS produced at the rear of the model is seen to move closer to the trailing edge helping to introduce high momentum fluid into the near wake. Observing the instantaneous vorticity generated by the 1 percent pre-tension membrane at 20° AoA, plot A of Figure 3-4 shows high momentum fluid building up on the lower surface of the membrane. This build up creates a pressure bubble that traverses down the membrane, then at the trailing edge the high pressure is released, plots B and C. The release of high pressure into the lower pressure region at the trailing edge causes a vortex structure of opposite sense (compared to the leading edge) to form, plot D. The vortex structure introduced at the trailing edge interacts with the shear layer reducing its overall size. These structures also introduce mixing into the near wake allowing higher momentum fluid to mix with lower momentum. While both membrane models had similar features the 1 percent pre-tension membrane seemed to slightly out perform the 4 percent pre-tension membrane based on the size of the separation bubble, shear layer height, and wake deficit. This is further supported by the results obtain by Zhang et al. [47] where force measurements were taken on identical membrane models. The 1 percent pre-tension membrane had a slight improvement in aerodynamic efficiency compared to the 4 percent pre-tension membrane model.

### **Membrane Surface Deflections**

The 3D surface membrane deflections were captured using the high speed DIC system discussed in the previous chapter. The intent of investigating the membrane surface deflections is to provide a better understanding of the membrane's motions and how it is affected by the fluid flow. All length scales with this section have been normalized by the full chord length. The membrane models will first be analyzed

qualitatively by looking at their mean deformations and RMS fluctuations. Further analysis will include trends on mean shape variations. Next, the PSD of the membrane's fluctuations in both the temporal and spatial directions will be investigated to further analyze the membrane's motions. Finally, correlations between spatial locations will be compared in an attempt to describe the wave like nature which the membrane moves in. Within each section, the synchronized DIC results will first be introduced followed by the later independent DIC results.

### **Mean and Root Mean Square Deflections**

The time averaged mean deflections of the membrane models were calculated via Equation 2-3. Figure 3-5 plots the mean deflections of both the 1 percent pre-tension model and the 4 percent pre-tension model through a range of AoAs: 4°, 8°, 12°, 16°, and 20°. The outer frame and battens for the membrane models have been superimposed in the contour plots to better help establish the orientation in which the membranes lie. Membrane models shared similar trends, both models experienced an increase in deflections as AoA is increased (increase in aerodynamic loading). One feature to note about the deflections is the asymmetric shape that the outer membranes exhibit (discussed later) whereas the middle membrane exhibits a symmetric distribution. The symmetric displacements at the middle membrane are similar to the results of the higher aspect ratio membrane models obtained by Timpe et al. [35] whose data was taken at the center membrane where 3D tip effects were thought to be of minimal influence. These similar traits can also be found in the independent DIC cases later investigated, Figure 3-6. One discrepancy to note is the deflections at the leading edge of the left membrane. After construction, the left membrane had a slight sag at static conditions. The sag at the leading edge allowed the membrane to have an

increase in deflection at that specific location. Normally, the area experiencing the sag should show minimal deflections, as in the synchronized case. As previously stated, the bulk deflections remained similar.

The membrane's fluctuations are shown in the RMS plots, Figure 3-5. Since the membrane models are BR and have scalloped trailing edges, both models experienced max fluctuations at the center trailing edge for all tested cases. While looking at the contour plots no clear trend stands out, however one item is noted, membrane fluctuations dramatically decrease after a certain AoAs. This decrease was also experienced in the independent DIC cases shown in Figure 3-6. Another similar feature was the greater fluctuations experienced at the outer edges of the left and right membranes. The wing tip vortices were thought to be the cause of these asymmetric fluctuations however the mounting hardware was also believed to be a contributing factor since the models were supported by the outer edges.

### **Effects of Mounting Hardware**

During both the synchronized and independent experiments the membrane models were supported by two airfoil shaped hangers, one at either side of the model, hangers can be seen in Figure 2-8. The mounting hardware was converted such that the models would now be supported at the center of the model by a single airfoil shaped hanger, Figure 2-10. This change was done to rule out any suspicions whether the outer supports were contributing to the asymmetric deformations. Normalized mean deflections and RMS plots of the center supported models are shown in Figure 3-7. Qualitatively looking at the plots, the presence of the asymmetry experienced at the outer membranes is just as defined as in the cases with the outer supported hardware. Mean deflection plots remain comparable however the RMS plots had a slight

increasing in fluctuations at the outer membranes. Even though the outer supports may have cause a slight decrease in fluctuations at the outer cells, bulk deflections as well as the asymmetric deformations still existed. These plots help support the hypothesis made earlier, stating the asymmetric deformations were caused by the wing tip vortices and not hardware induced.

### **Mean and Root Mean Square Deflections Along the Mid-Plane**

To obtain a better understanding of the membrane surface changes with AoA, deformations along the midpoint of each membrane are investigated. Figure 3-8 plots the normalized mean deflections of the left, middle, and right membranes at their respective geometric centers as a function of AoA. Additionally, within the plots are error bars which represent the normalized RMS fluctuations at the same midpoint location. Furthermore, both sets of synchronize DIC data and independent DIC data have been included, columns A and B respectively. When comparing the membrane models it becomes evident that pre-tension has a significant effect on the membrane's deflections. The 1 percent pre-tension membrane allows for greater flexibility throughout all AoAs compared to the 4 percent pre-tension model. Looking at the RMS fluctuations at 8° AoA for all plots, there exists an induced excitation that leads to an increase in fluctuations. At higher AoAs ( $\alpha > 20^\circ$ ) the membrane's fluctuations significantly decrease. The decrease in fluctuations is a byproduct of the increased aerodynamic loading causing the membrane to stretch, thus not allowing the membrane to oscillate as freely. When comparing the synchronized data to the independent DIC data, a slight discrepancy in RMS fluctuations is noted. While the trend of RMS fluctuations generally remained the same the fluctuations in the independent case experienced a noticeable decrease in magnitude. Even though the RMS fluctuations did not agree between data

sets the magnitude of the mean deflections reasonably agree. The discrepancy in the RMS fluctuations is thought to be a byproduct of the new stiffer mounting arm. The stiffer mounting arm was thought to decrease the amplitude of the membrane oscillations while still allowing a mean deflection due to the aerodynamic loading, however a further investigation will need to be conducted.

One of the aerodynamic benefits from the use of a passively compliant membrane is the camber associated with its flexibility. Figure 3-9 and Figure 3-10 plots the time averaged mean camber for both membrane models (synchronized DIC data is shown in Figure 3-9 and independent DIC data is shown in Figure 3-10). Averaged mean camber is plotted at the center chord for the middle membrane. As shown in the normalized mean deflection plots, camber increases with AoA. Both data sets and pre-tensions have similar features in the presence of a pressure difference. The 1 percent pre-tension membrane is able to increase its camber on average 2.3 times greater than the 4 percent pre-tension membrane. Max deflection tends to be closer at the leading edge of the models at lower AoAs. When AoA is increased, a transition of max deflection occurs, shifting the max closer to the trailing edge. At the higher AoAs ( $\alpha > 20^\circ$ ) the average mean camber for each model tends to level off reaching a constant camber. The constant camber suggests the models have reached their respective material limits.

### **Power Spectral Density and Membrane Motion**

The membrane motions have further been examined by looking at the trailing edge fluctuations. The frequency power spectrum was calculated using Equation 2-7. Figure 3-11 shows the PSD obtained at the center of the trailing edge of each membrane cell (left, middle and right) for the 1 percent pre-tension membrane column A

and the 4 percent pre-tension membrane column B. While only AoAs of  $8^\circ$ ,  $12^\circ$ , and  $16^\circ$  are shown, angles of  $4^\circ$ ,  $20^\circ$ ,  $24^\circ$ ,  $28^\circ$ , and  $32^\circ$  exhibits similar feature and their graphs have been omitted. A discussion of the full range of AoAs is soon to follow. The different cells within the 1 percent pre-tension model all tend to experience the same dominate frequency disregarding the  $8^\circ$  AoA. At the  $8^\circ$  AoA the middle membrane seems to experience a peak shifting phenomena, shifting it's dominate frequency slightly higher. Each cell within the 4 percent pre-tension model also experiences the same dominate frequency as each other. Furthermore, an additional peak at a higher frequency is also present throughout all AoAs. The additional peak experienced within the PSD is thought to be contributed to the RMS fluctuations, where the membranes are seen to have two distinct peaks in the RMS plots. Again, at  $8^\circ$  AoA the higher frequency experiences a slight peak shifting phenomena.

Using the PSD for each model, Figure 3-12 and Figure 3-13 plot the membrane's first dominate frequency as a function of AoA. Synchronized DIC data is shown in Figure 3-12 and independent DIC data is shown in Figure 3-13. From these plots one can observe the effects of both the pre-tension and the added aerodynamic tensioning as the wing is brought to higher AoAs. The 1 percent pre-tension membrane tends to have a lower frequency compared to the 4 percent pre-tension membrane as one would expect based on a higher tension in the membrane. Furthermore, there is a general trend in the frequency of the membranes, where frequency increases with increasing AoA. This is expected as the aerodynamic load increases the membrane's tension with increasing AoA. While the flow provides the excitation for the membranes, the membrane's properties drive its motion, not shedding from the wing, which has been

reported for some cases of fully supported membrane wings [19], [48]. As the models AoA is further increased the membrane's oscillations levels off where again the membranes seems to have reached their material limits.

The membrane's motions were again examined by looking at the trailing edge fluctuations, however, this time they were observed qualitatively. Figure 3-14 plots the center trailing edge fluctuations for the 1 percent pre-tension model at AoAs of 4°, 12°, and 20°. Comparing the different cells within the model (left, middle, and right) at low AoAs the membranes appear to be randomly phased. They are thought to have started their cycles of oscillations and randomly come in and out of phase with each other. However, at higher AoAs, where there is a stronger aerodynamic loading present, the membranes are seen beating with each other and appear to be in phase. Continuing examining the membrane models qualitatively, Figure 3-15 plots a segment of instantaneous membrane surface fluctuations at the center chord of the middle cell. These instantaneous snapshots are used in calculation of the time averaged mean camber shown in Figure 3-10. The vertical axis within Figure 3-15 represents the chordwise direction of the model, while the horizontal axis represents time in milliseconds. The plots are for the 1 percent pre-tension membrane model at AoAs of 4°, 12°, and 20°. Similar behavior can be seen at other AoAs as well as in the 4 percent pre-tension membrane model. The normalized deflections visually show the wave type behavior of the membrane's motion. The motions display features of both a standing wave and traveling wave. A pure standing wave would plot straight vertical lines of alternating colors, portions of a standing wave can be seen in the upper regions of the plots (near the trailing edge of the model). A pure traveling wave would plot diagonal

lines of alternating colors, this can be seen in the middle portion of the plots (mid-chord of the model). While these plots visually show the membrane's motion is a combination of a standing wave and a traveling wave, a more detail description was desired.

A Fourier transform into wave number space was computed to obtain the wavelength of the traveling wave. The PSD was again calculated using Equation 2-7 this time in the spatial direction. Figure 3-16 plots the PSD for the 1 percent pre-tension membrane at AoAs of 8° and 16°. Examination of the plots conclude the PSD could not resolve a dominate spatial frequency for the membrane. The signal is thought to be likely aliased due to the poor spatial resolution. The bin size for the PSD calculated by Equation 2-6 equaled  $0.022 \text{ mm}^{-1}$ . With a spatial frequency of  $0.022 \text{ mm}^{-1}$  the largest wavelength that can be resolved is a 45.5 mm wave. What can be taken from these plots is the membranes do have a “small” ( $<0.022 \text{ mm}^{-1}$ ) spatial frequency which translates to the membrane having a wavelength larger than ( $>45.5 \text{ mm}$ ). Using Equation 3-2 where  $F$  is the dominate temporal frequency and  $\lambda$  is the wavelength, the membrane models have a wave speed of at least 2.61 m/s. Again, a more detailed description of the membrane's motion was sought after.

$$V = F * \lambda \quad 3-2$$

## Wave Speed

One of the goals within this investigation was to explain the wave like nature of the membranes. A correlation between the spatial locations was calculated by Equation 2-8. Each spatial location along the center chord was compared to the first spatial location. Figure 3-17 plots the results of the correlations for the 1 percent pre-tension model at 8° AoA. Plot A shows the autocorrelation of the first spatial location at

$x/c=0.22$ . As the correlation plots continue, the spatial distance is incremented by 20 spatial locations (equivalent to 0.14 in the nondimensional length scale). Plots B and C both show a shift in peak correlation stating the membrane is behaving like a traveling wave. The additional peaks at both  $\tau = \pm 13$  are due to the periodic characteristics of the signal. One interesting feature that all membrane models exhibit is a temporary transition to a standing wave. Examining plots C and D, where the correlation compares the  $x/c=0.5$  location and  $x/c=0.64$  location, the correlation remains relatively stationary. This stationary portion of the correlation resembles that of a standing wave. This notion of a standing wave can be further supported by Figure 3-18. This figure shows the membrane's motion through one cycle of oscillations for the 1 percent pre-tension model at  $12^\circ$  AoA. Within the oscillations, there exists one position where the membrane typically passes through. This point can be thought of as a type of node where two traveling waves intersect and cancel each other. At this intersection the sum of the waves is approximately zero. Reverting back to Figure 3-17, plot E shows the correlation at the  $x/c=0.78$  location. The correlation slightly changes, however the membrane returns to the trend of a standing wave.

Using the data from the correlations analysis and knowing the distance between each spatial location along with the time between each signal, a wave speed for each membrane can be calculated. To help resolve some of the ambiguity in picking a tau, a least squares method was applied to the correlations previously obtained. The results of this method can be seen in Figure 3-17, where the red line represents the new approximated correlation. Wave speeds were obtained at 15 different spatial locations and averaged. Figure 3-19 plots the average wave speed as a function of AoA for both

membrane models. The 4 percent pre-tension membrane produced higher wave speeds throughout all AoAs as one would expect based on the higher tension in the membrane. At the lower AoAs, the higher wave propagation is thought to be due to the location of the shear layer. Since the shear layer is relatively close to the membrane's surface, some of the higher free stream velocity is entrained and transitioned into the membrane aiding in the wave speed. As the AoA is increased, the shear layer grows in both size and height, thus not allowing the higher momentum fluid to reach the membrane's surface. The wave propagation relies on the tensioning within the membrane as well as the tensioning associated with the increase in aerodynamic loading. As AoA is increased the membrane's frontal projection area is also increased, this allows a larger portion of the membrane to experience an increase in loading. This increase in loading is proportional to the tensioning within the membrane where an increase in tension leads to an increase in wave speed.

### **Fluid Structure Interactions**

The synchronization of the flow-field fluctuations and membrane oscillations highlighted some of the couplings associated with the membrane and flow. Since PIV and DIC were acquired simultaneously, both of their respective PSD's are compared. The PSD of the flow-field was obtained in the same fashion as in the membrane's PSD. Figure 3-20A shows the normalized U-component of the velocity field for the 1 percent pre-tension membrane model at 8° AoA. The diamond shapes signify the locations where PSD was calculated. Figure 3-20B plots the PSD at each of the diamond locations along with the previously found PSD of the middle membrane's trailing edge. One of the main features in Figure 3-20B is the presence of the membrane's dominate frequency appearing throughout the flow-field. This suggests the membrane motions

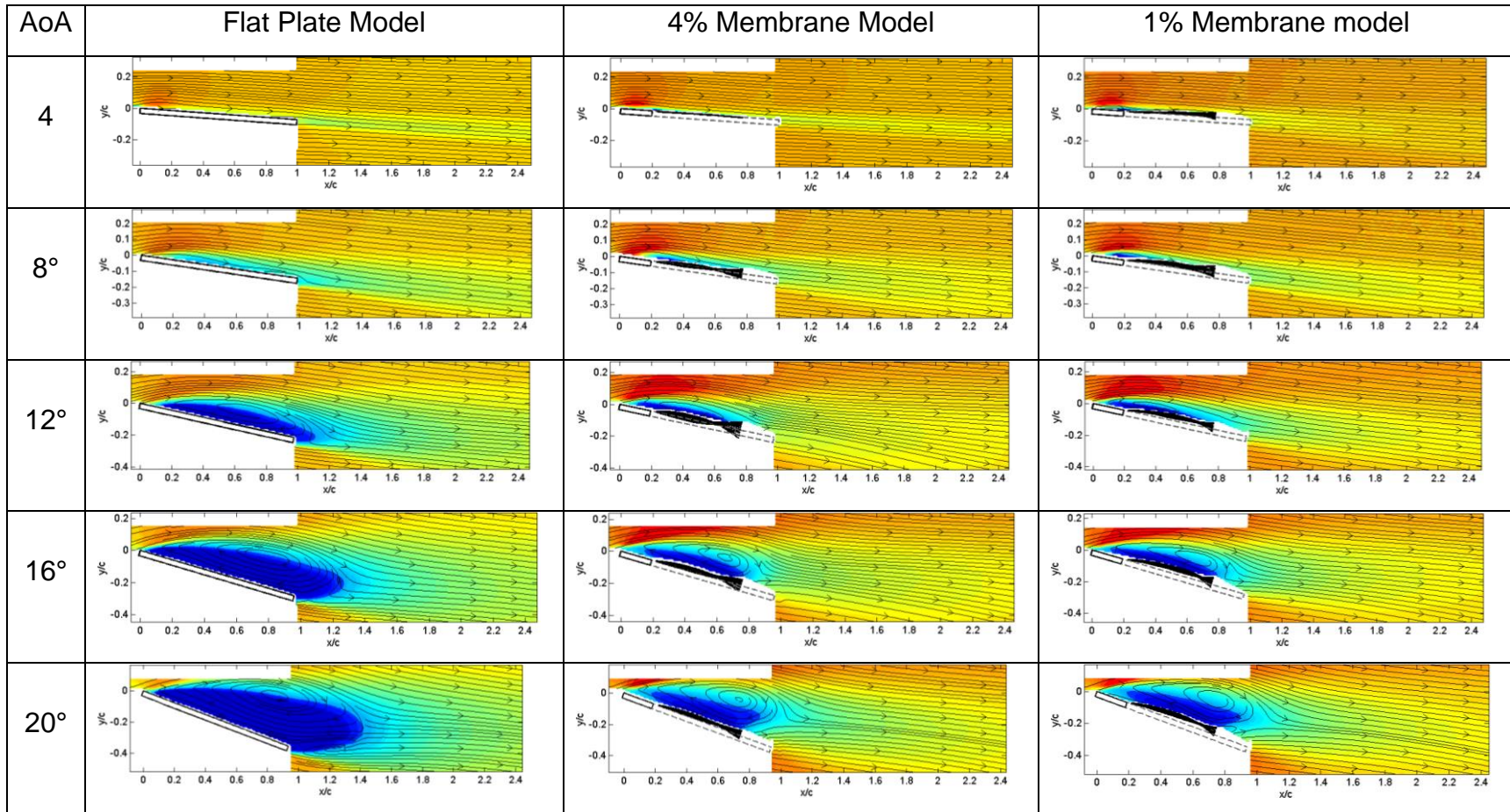
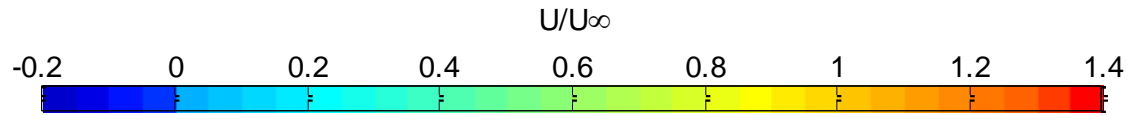
are driving the surrounding flow-field. The powers associated with the flow-field's dominate frequency are dependent upon location relative to the membrane. Powers at the leading edge are significantly less than the powers associated with the flow around the trailing edge and near wake. The near wake provides the highest powers due to the large fluctuations experienced within the U-component of velocity. Figure 3-21 plots the PSD of the velocity field's fluctuating U-component at the  $x/c=1.0$  and  $x/c=2.0$  locations for AoAs of  $12^\circ$ , and  $16^\circ$  (plots A and B respectively). Although the higher frequencies of the velocity spectra are likely aliased due to the spatial resolution of the PIV, one can still clearly resolve a peak in the spectra. While the results for the  $4^\circ$  and  $20^\circ$  AoAs along with 4 percent pre-tension are not shown, these cases also exhibit similar behaviors. The membrane's dominate frequency appears throughout the flow-field while higher powers are seen in the trailing edge and the near wake of the models.

The Strouhal number for the membrane models was then investigated. This nondimensional number is used for describing oscillations within fluid flow. Equation 3-3 shows a modified Strouhal number where  $F$  is the wake frequency,  $L$  is the projection length of the model, and  $V$  is the freestream velocity. Using the membrane's dominate frequency previously found as the flow-fields dominate frequency, the modified Strouhal number is evaluated. Figure 3-22 plots the modified Strouhal number vs. AoA for both membrane models. Additionally within the plot is an approximate Strouhal number ( $St \approx 0.17$ ) where Fage and Johansen [49] showed for a rectangular flat plate at lower AoAs ( $\alpha < 30^\circ$ ) the modified Strouhal number varied between 0.15-0.22. Examining Figure 3-22, the Strouhal number increases with increases AoA until  $28^\circ$  where it then starts to decrease. This decrease is thought to be a byproduct of the models reaching

their material limits. Comparing the membrane models trend to the trend obtained by Fage and Johansen, the membrane models appear to driving the surrounding flow significantly altering it from a traditional rectangular flat plate model.

$$St = \frac{fL}{V} \text{ where } L = \text{chord} * \sin(\alpha)$$

3-3



A

B

C

Figure 3-1. Normalized mean U-component of the flow-field with streamlines for the different models. Column A) flat plate model. Column B) 4 percent pre-tension model. Column C) 1 percent pre-tension model.





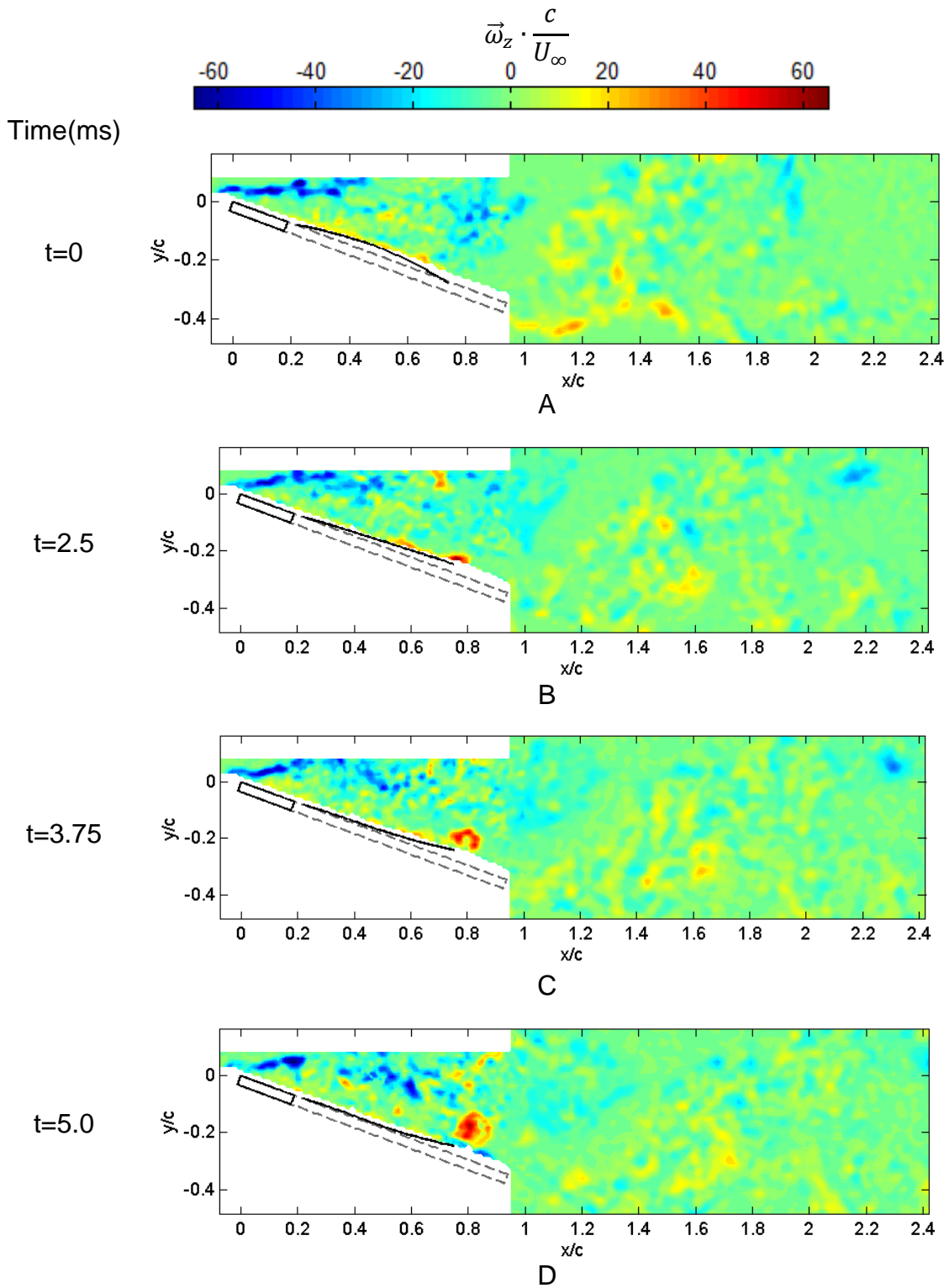


Figure 3-4. Normalized instantaneous vorticity for the 1 percent pre-tension membrane at 20° AoA.

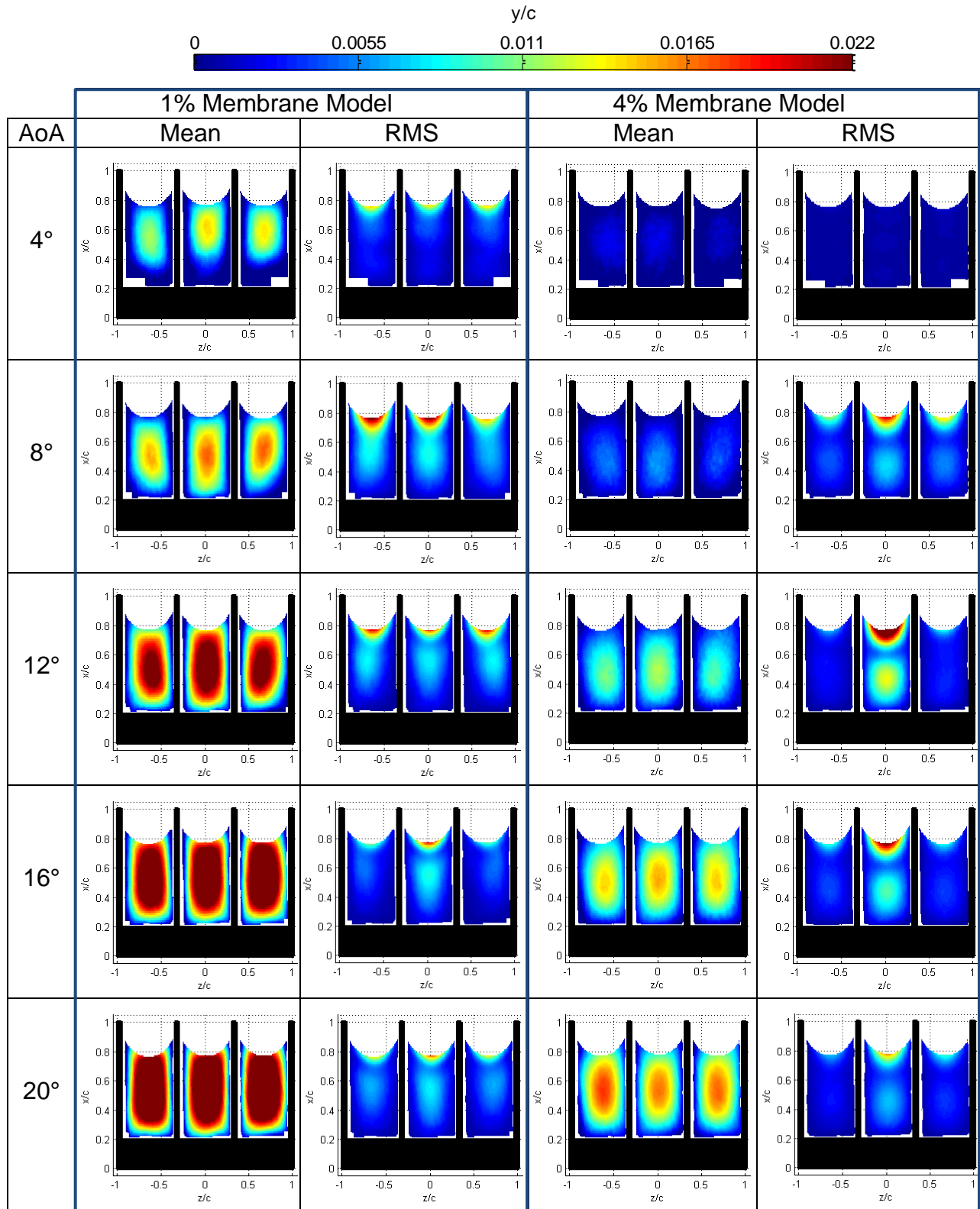


Figure 3-5. Normalized mean membrane deflections and normalized RMS deflections through a range of AoAs for the synchronized data.

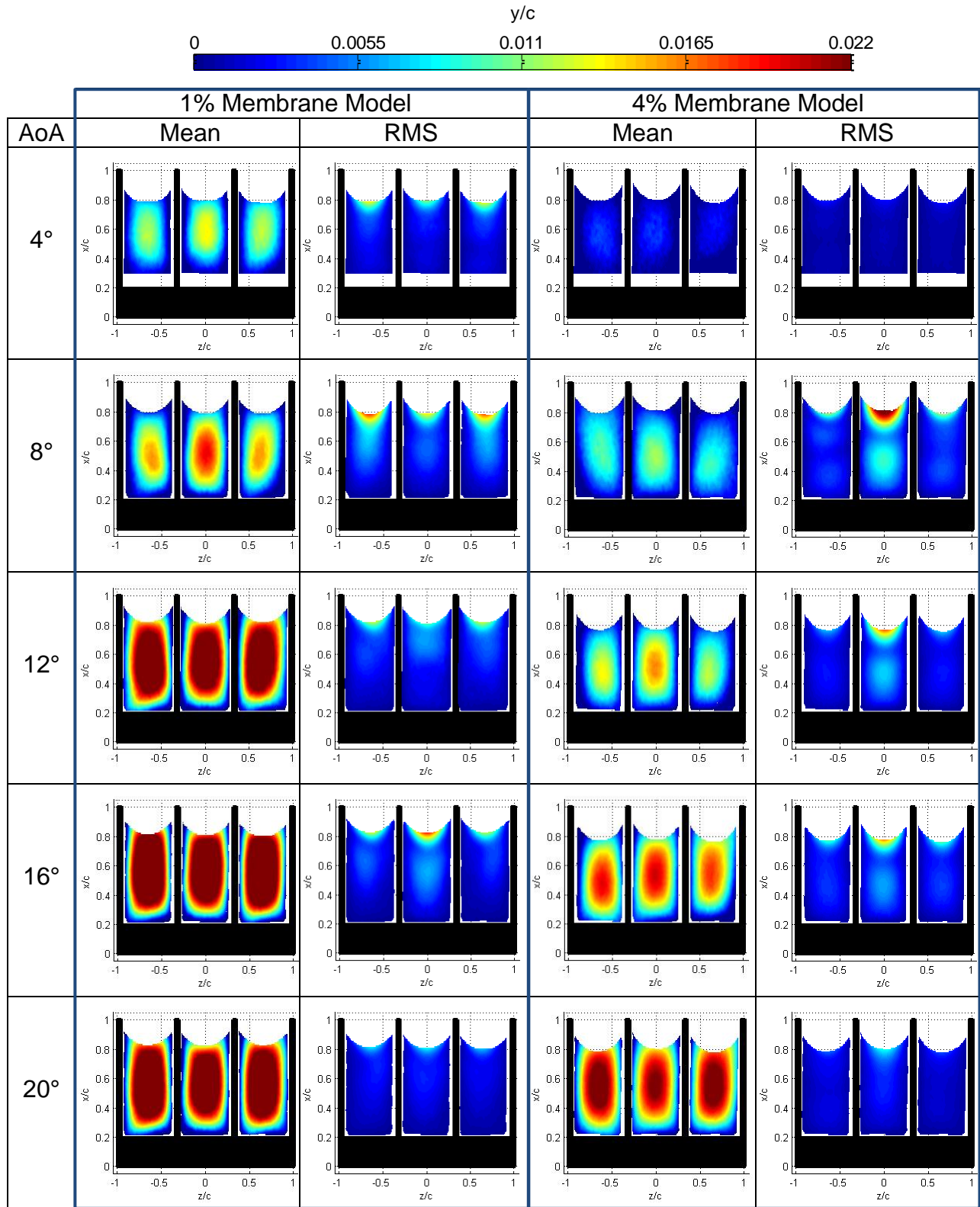


Figure 3-6. Normalized mean membrane deflections and normalized RMS deflections through a range of AoAs for the Independent DIC data with outer supported models.

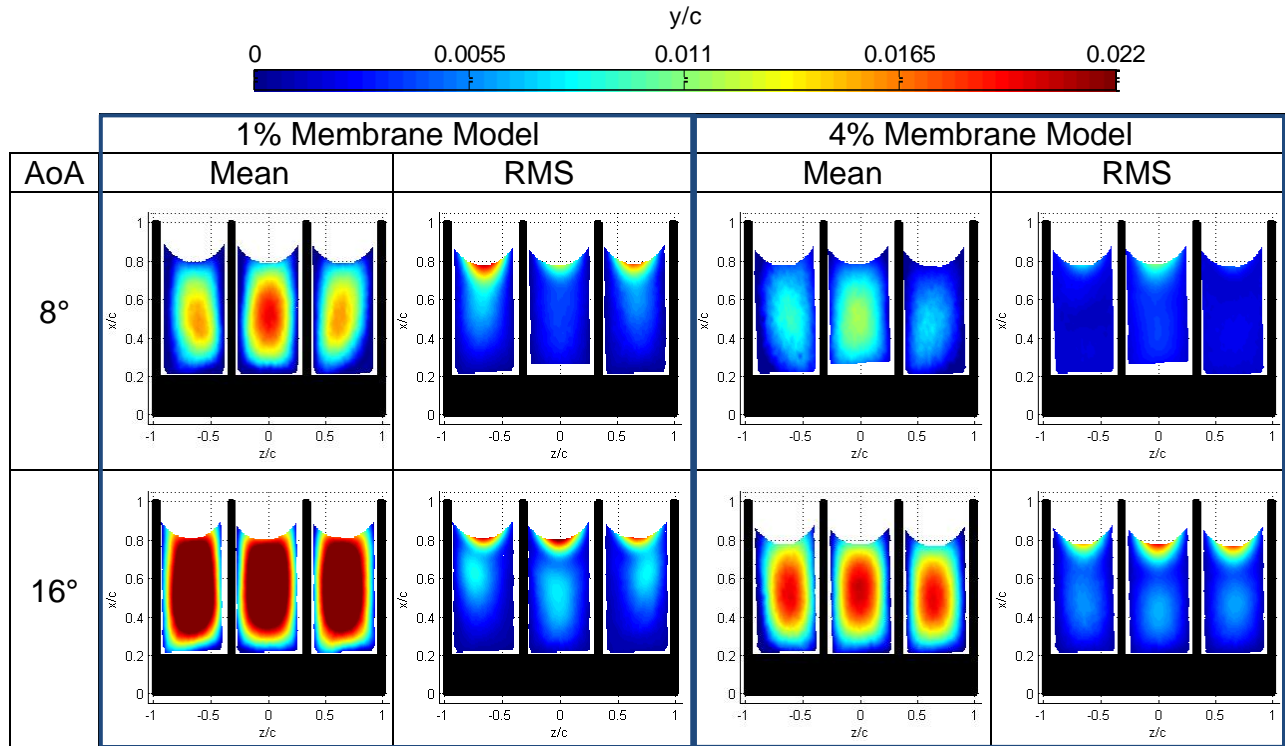


Figure 3-7. Normalized mean membrane deflections and normalized RMS deflections through a range of AoAs for the Independent DIC data with center supported models.

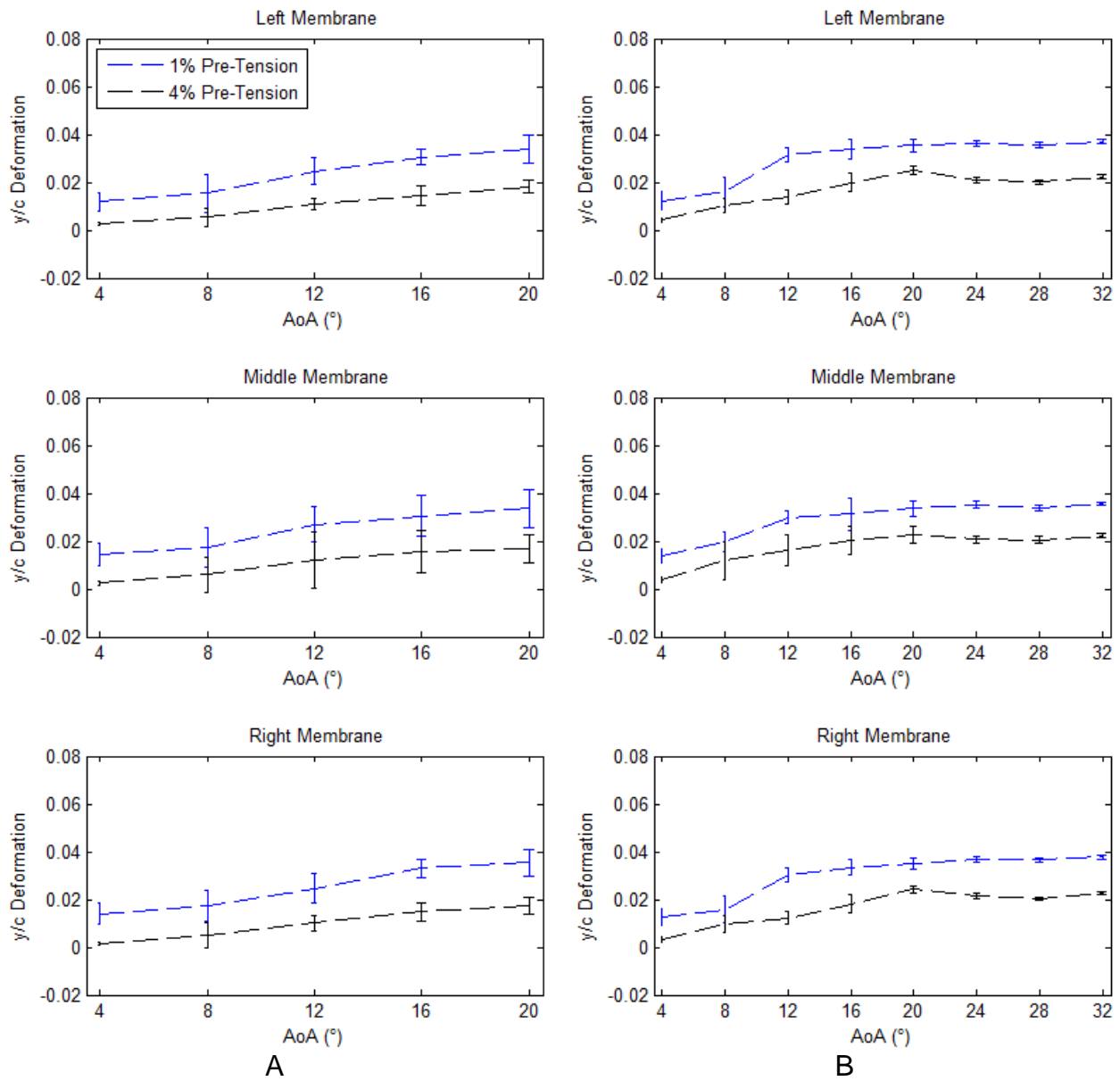


Figure 3-8. Membrane's center normalized mean and RMS deflections vs. AoA. Column A) Synchronized data. Column B) Independent DIC data.

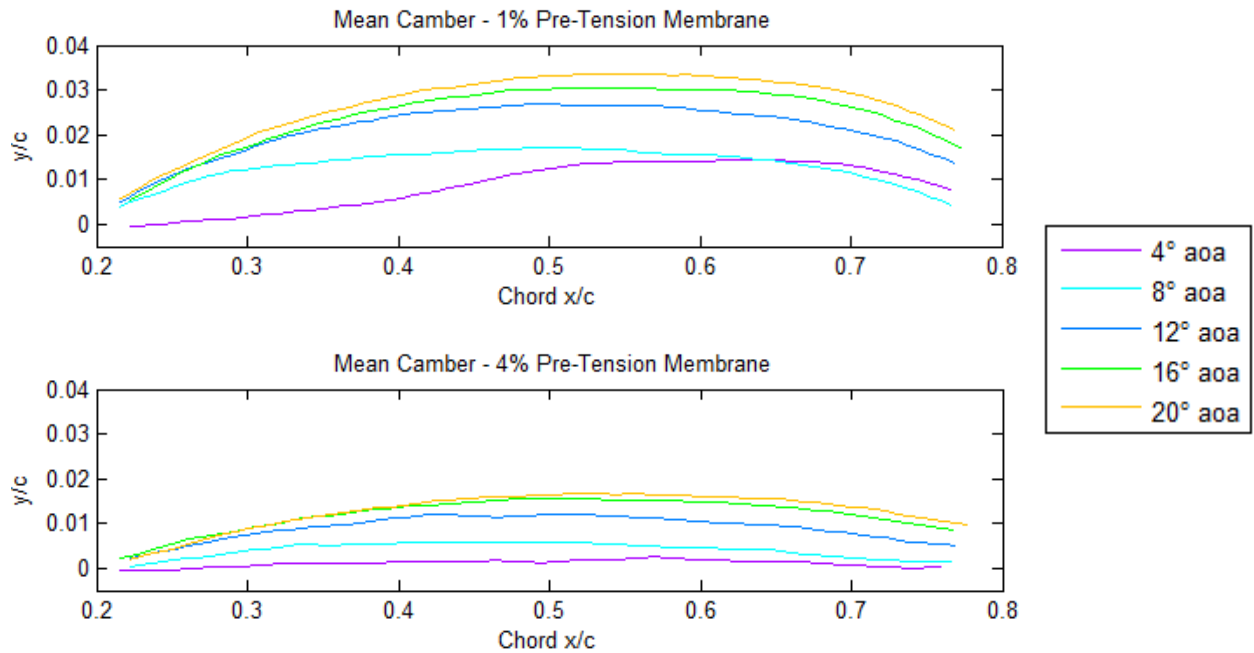


Figure 3-9. Time averaged mean camber of middle membrane for the synchronized data.

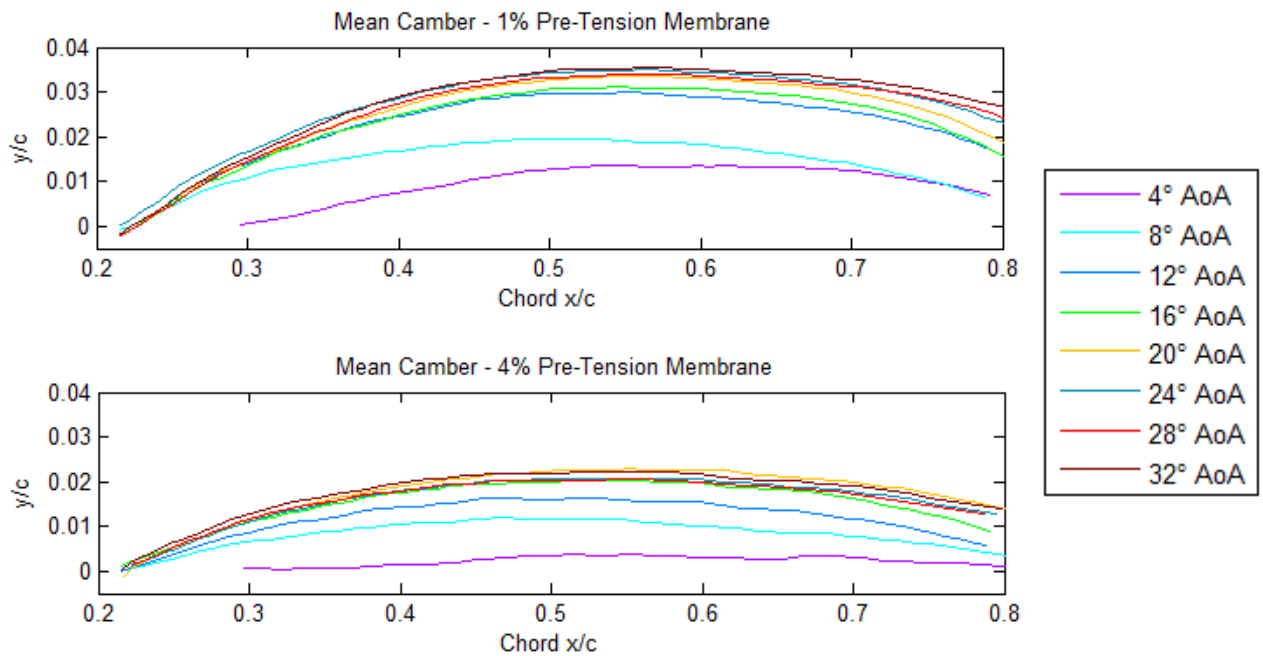


Figure 3-10. Time averaged mean camber of middle membrane for the independent DIC data.

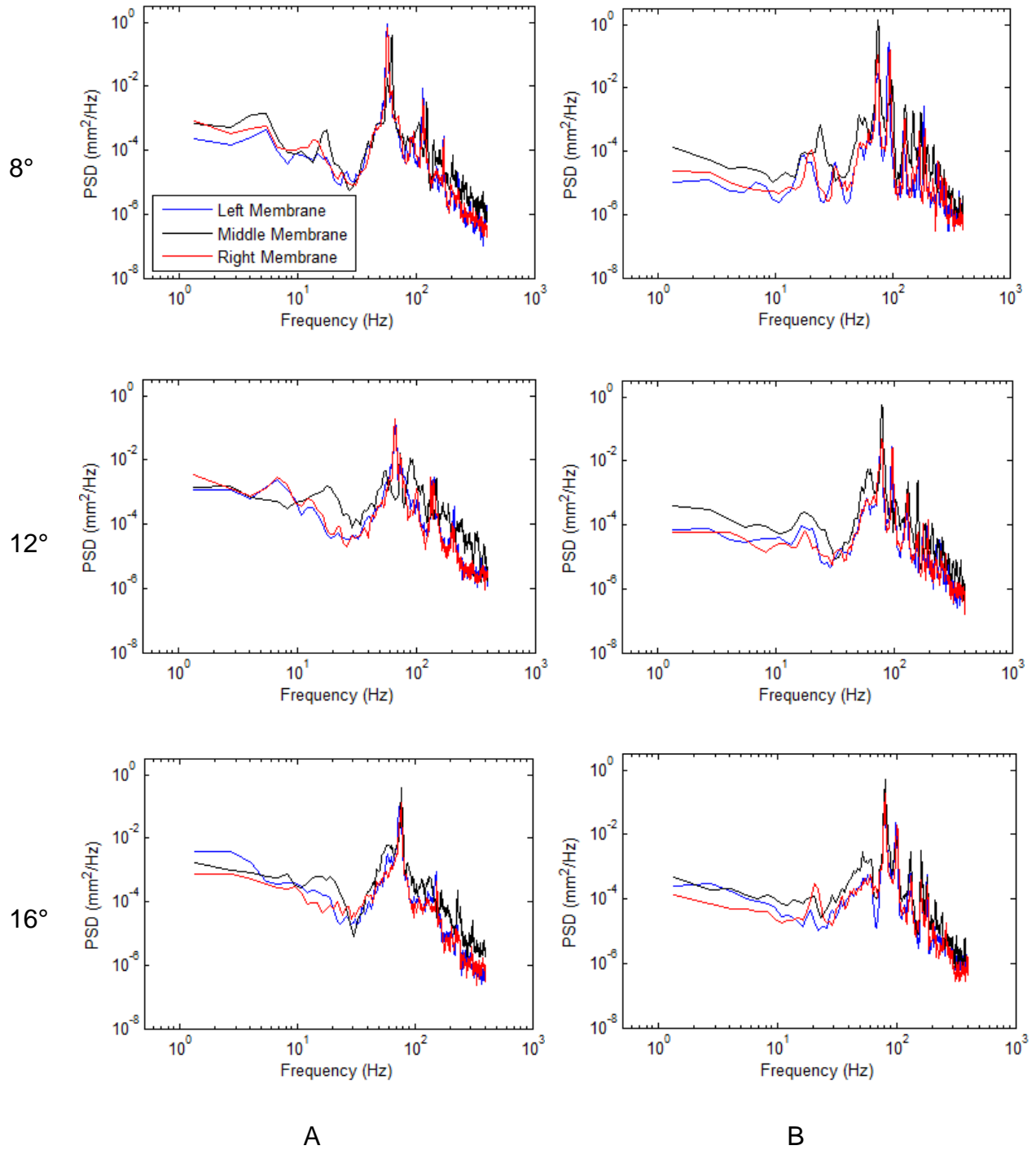


Figure 3-11. Trailing edge PSD for each membrane. Column A) 1 percent pre-tension membrane model. Column B) 4 percent pre-tension membrane model.

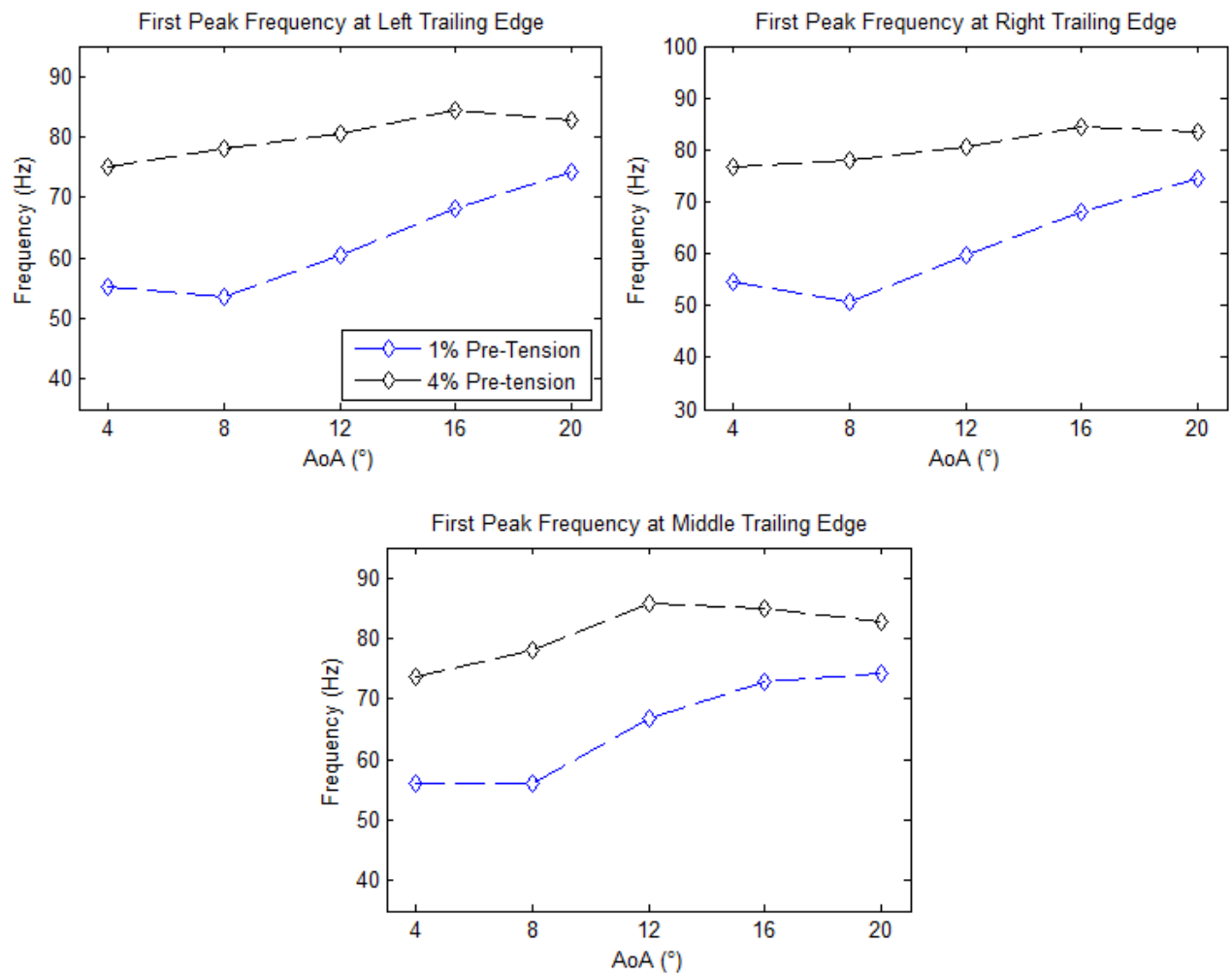


Figure 3-12. First dominate frequency vs. AoA for each membrane during synchronized testing.

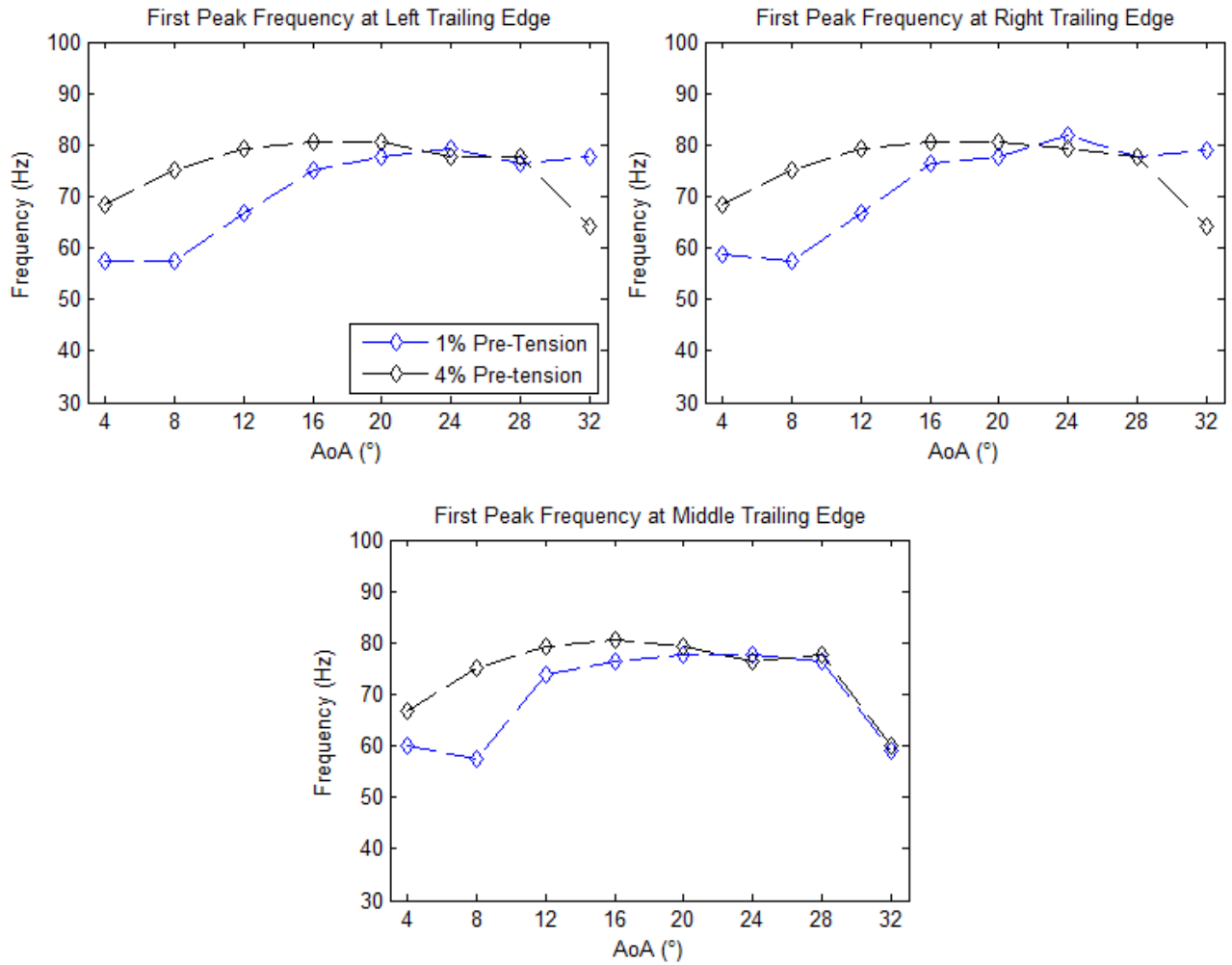


Figure 3-13. First dominate frequency vs. AoA for each membrane during independent DIC testing.

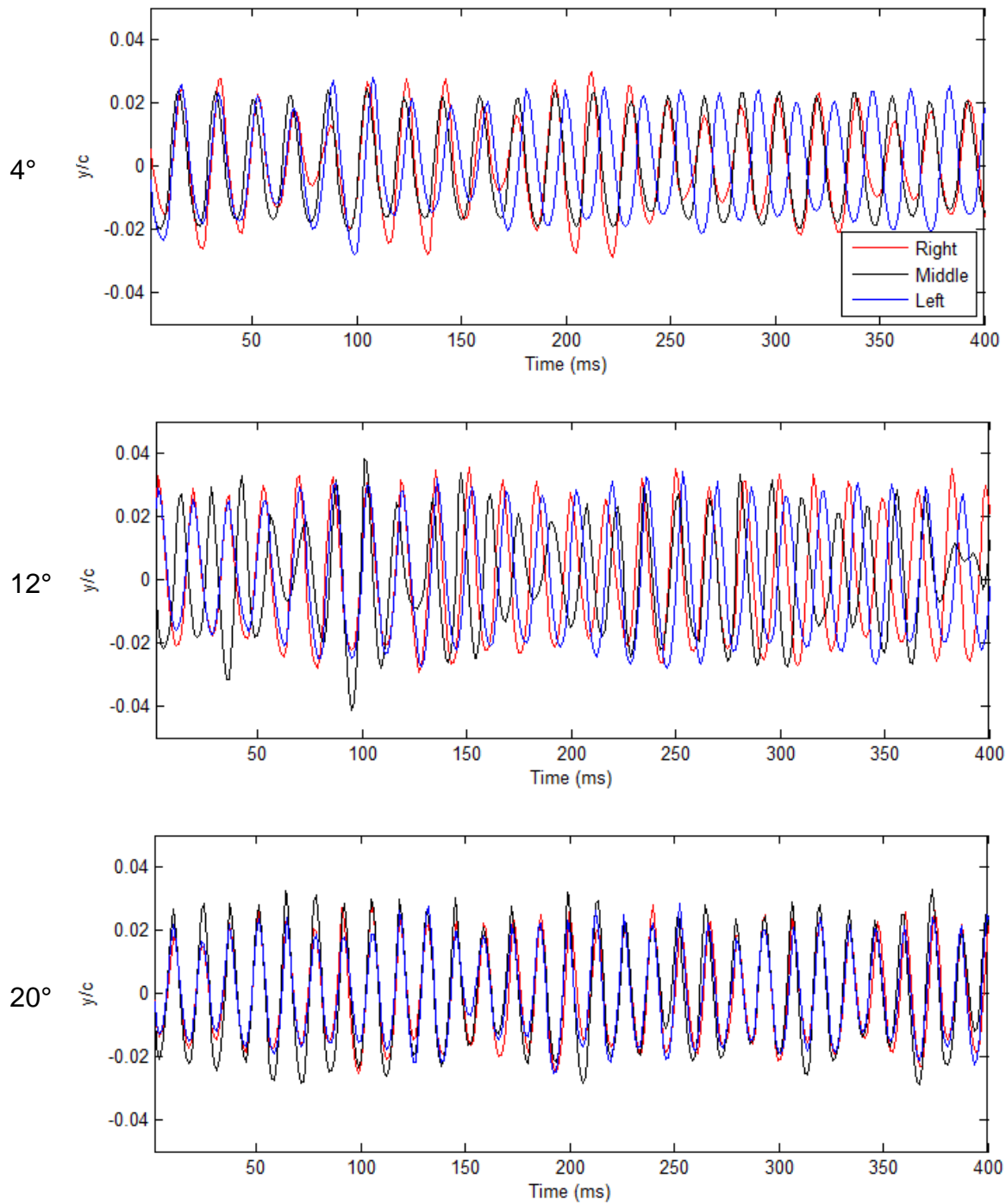


Figure 3-14. Instantaneous trailing edge membrane surface deflections for the 1 percent pre-tension membrane model.

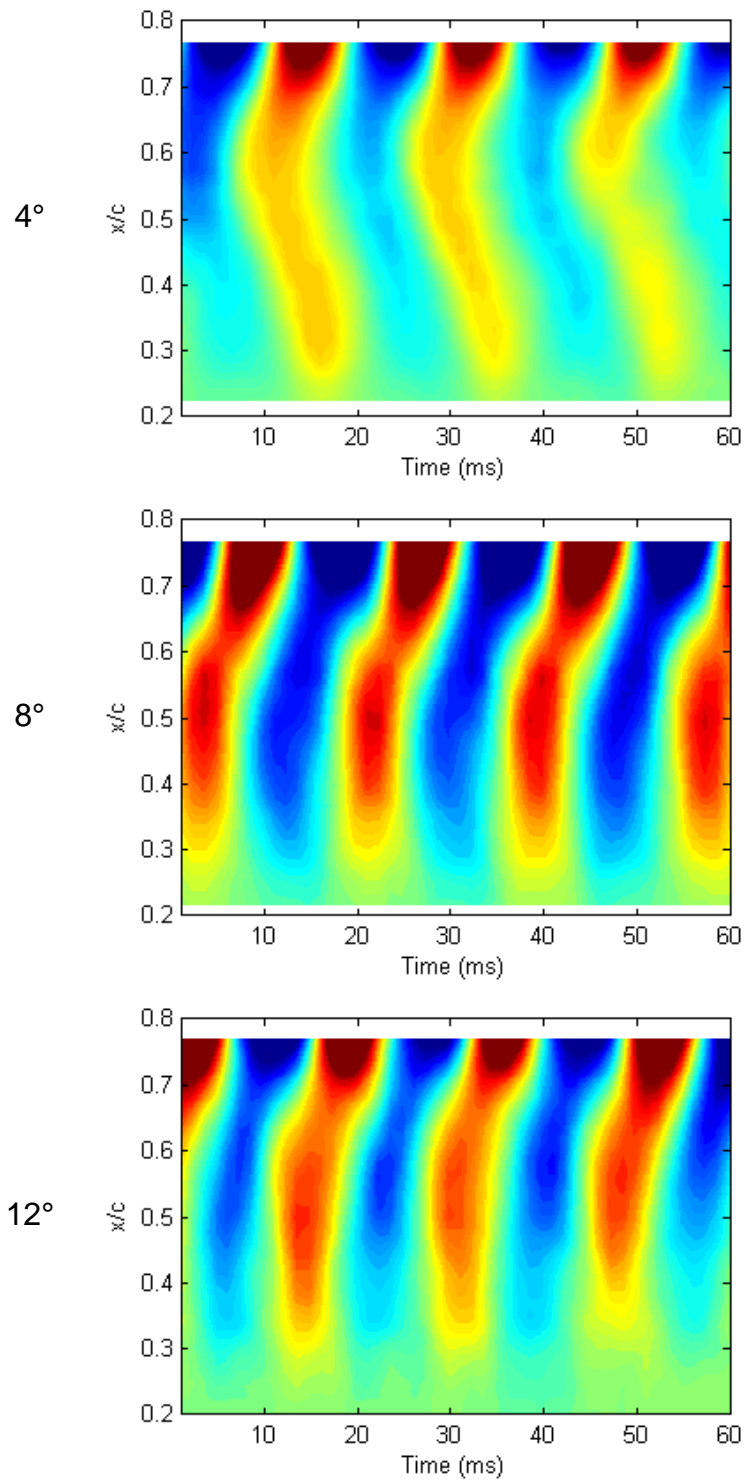


Figure 3-15. Instantaneous center chord membrane surface deflections for the 1 percent pre-tension membrane model.

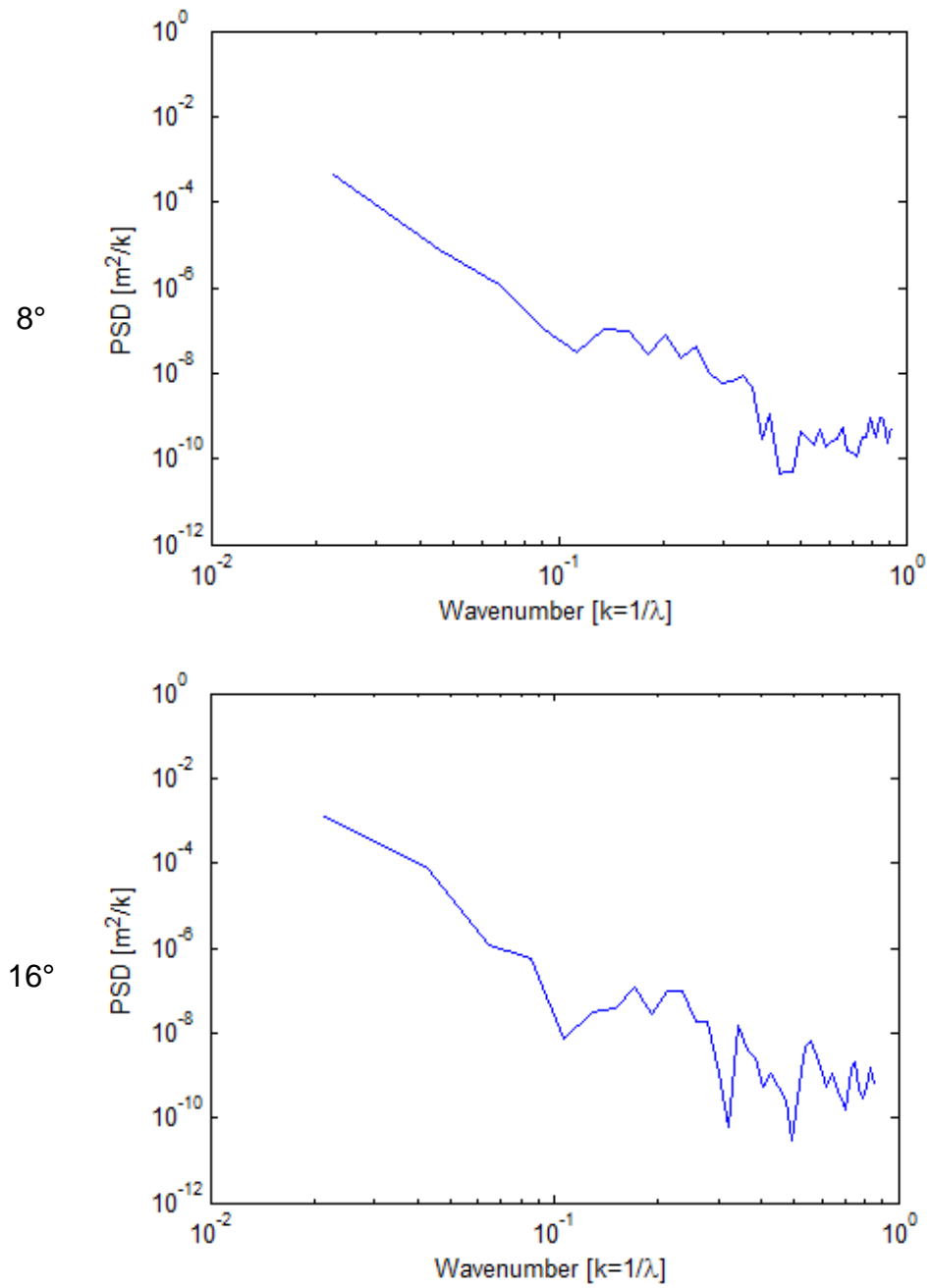


Figure 3-16. PSD in the spatial domain.

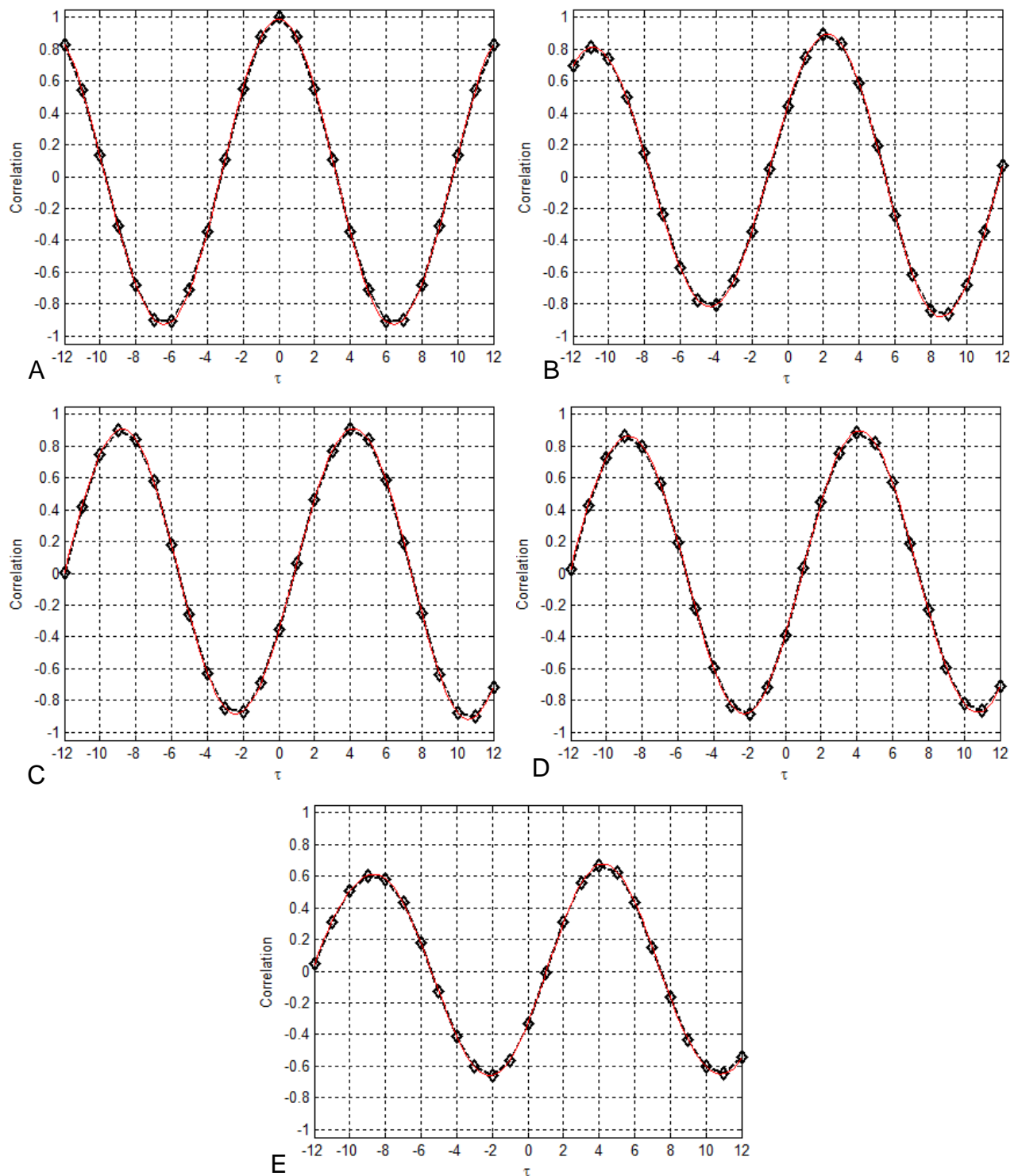


Figure 3-17. Cross correlations between spatial locations for the 1 percent pre-tension membrane at 8° AoA. Plot A) Autocorrelation at  $x/c= 0.22$  location. Plot B) Cross correlation at  $x/c= 0.36$  location. Plot C) Cross correlation at  $x/c=0.5$  location. Plot D) Cross at  $x/c=0.64$  location. Plot E) Cross correlation at the  $x/c=0.78$  location.

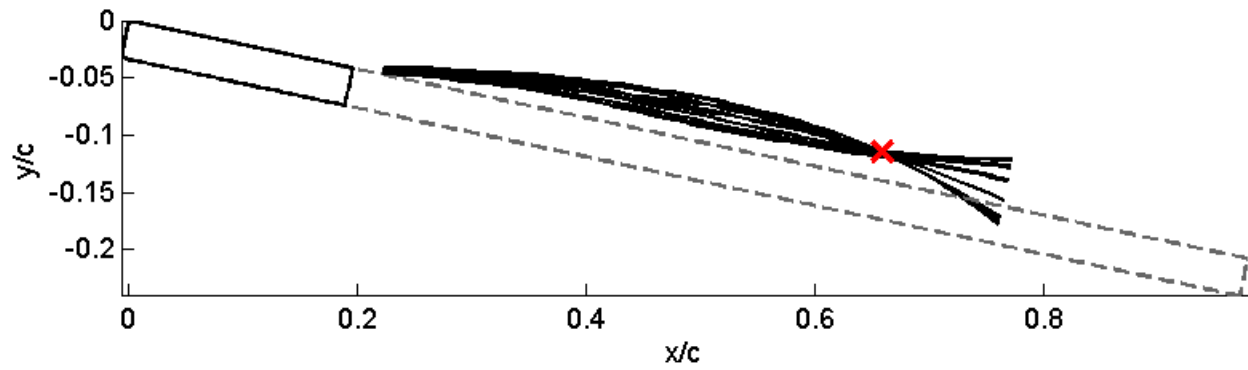


Figure 3-18. Membrane oscillations for the 1 percent pre-tension model at 12° AoA. Red 'X' approximates the location where two traveling waves intersect and cancel each other.

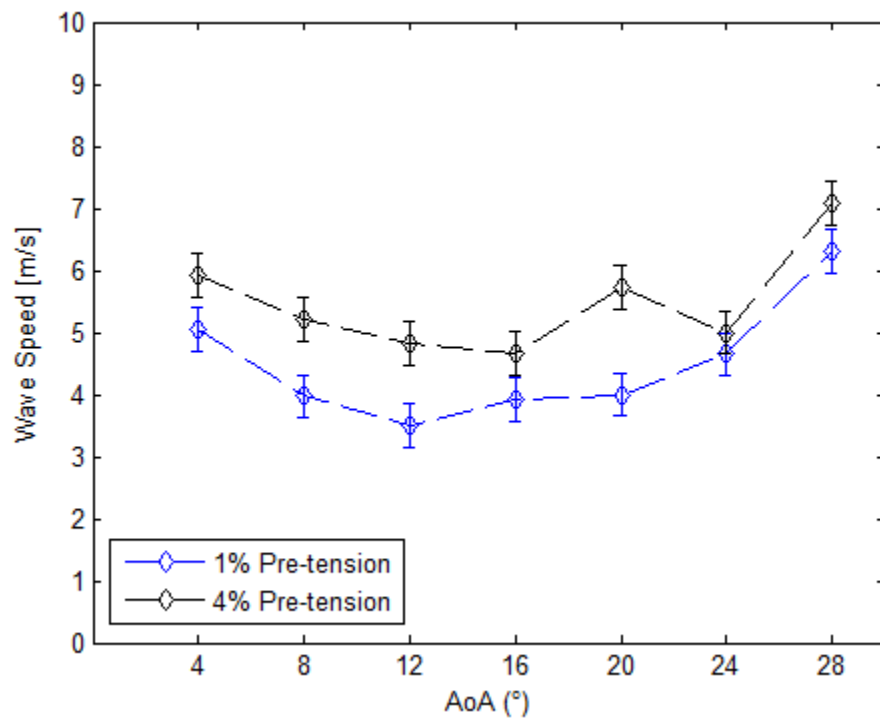


Figure 3-19. Middle cell average wave speed vs. AoA for both membrane models.

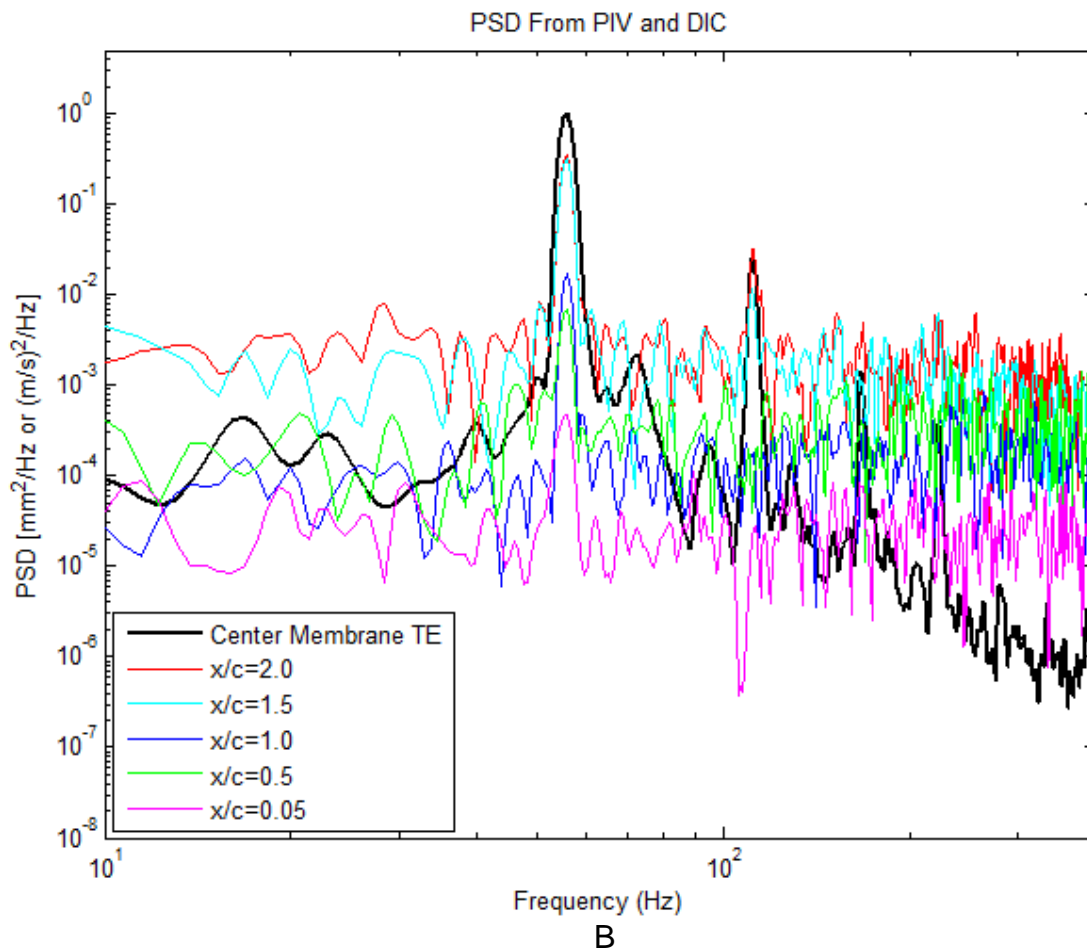
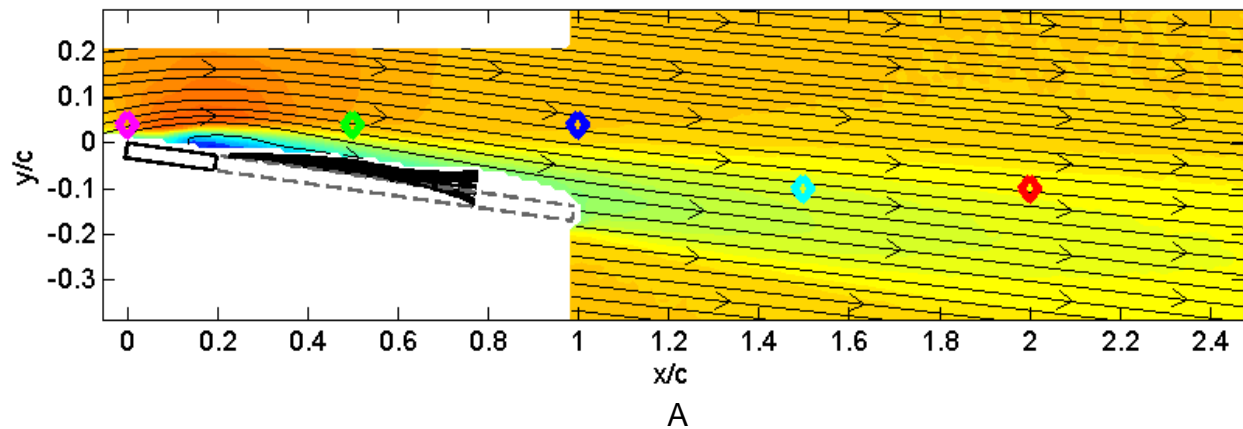
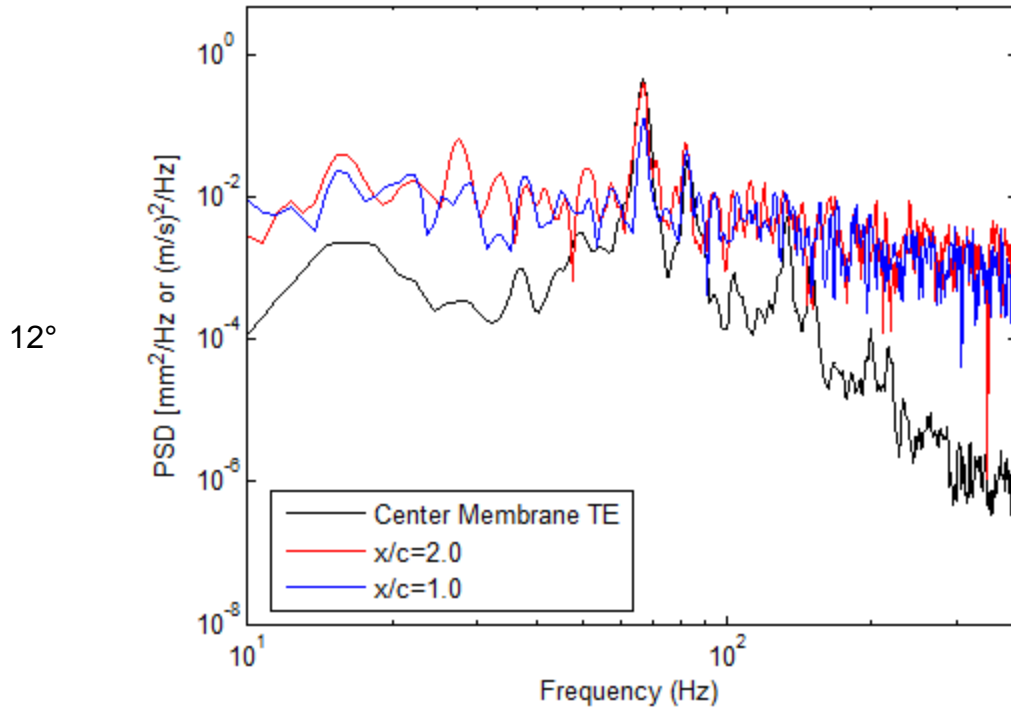
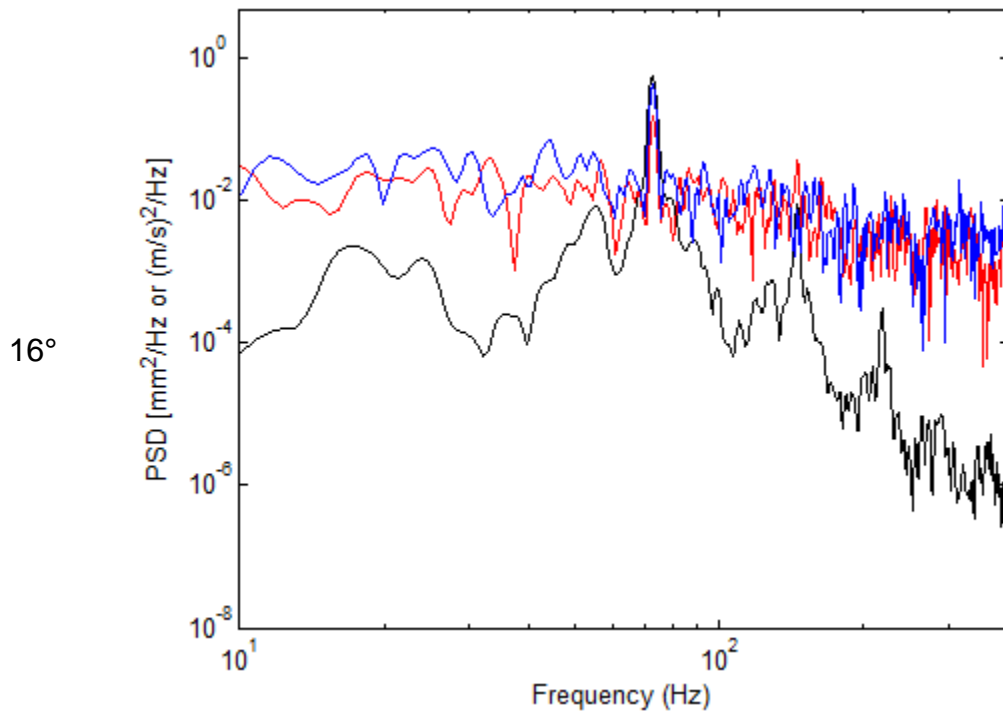


Figure 3-20. PSD of both the middle membrane's trailing edge and select locations of the flow-field for the 1 percent pre-tension membrane at  $8^\circ$  AoA. Plot A) U-mean plot specifying the exact locations where PSD was obtained at. Plot B) Plots the PSD of the specified locations in plot A, along with the PSD of the middle membrane's trailing edge.



A



B

Figure 3-21. PSD of both DIC and PIV for the 1 percent pre-tension membrane model. Plot A) 12° AoA. Plot B) 16° AoA.

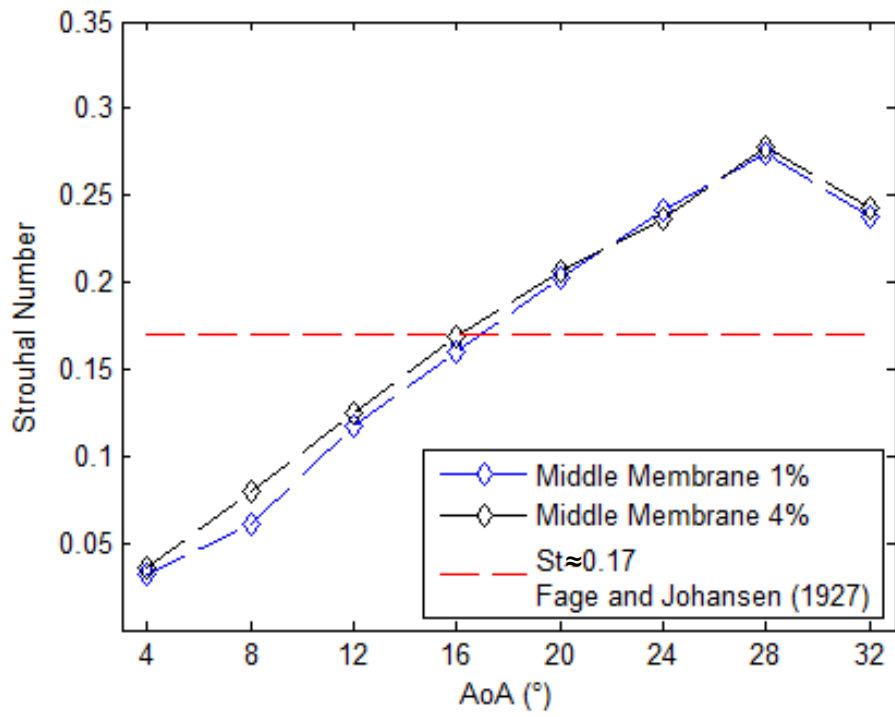


Figure 3-22. Modified Strouhal number vs. AoA.

## CHAPTER 4 SUMMARY AND FUTURE WORK

This study investigated both the fluid and structure characteristic of a low aspect ratio, batten reinforced, multi-cell, scalloped membrane wing in a low Reynolds number flow. Two different membrane models were investigated, the first model had a 1 percent pre-tension membrane while the second model had a 4 percent pre-tension membrane. A time resolved PIV system was synchronized with a high-speed DIC system allowing the streamwise flow-field and 3D membrane surface deformations to be captured simultaneously. Analysis of the data resulted in structural dynamics of both the membrane oscillations and the unsteady flow-field measurements. This was followed by another investigation consisting only of independent DIC data. While the independent DIC data was conducted in a different facility, the experimental set-up remained relatively similar to the synchronized set-up. Analysis of this data set resulted in similar structural dynamics of membrane oscillations as in the synchronized data. Furthermore, the wave like motion of the membrane's movements was explored.

### **Summary**

Time averaged flow-fields of both membrane models and a flat plate model were obtained by PIV. Examining the normalized U-component of the flow-field even at low AoA ( $\alpha < 12^\circ$ ), it was apparent the membrane models have more desirable flow features than that of a flat plate. The membrane models had a noticeable increase in flow velocity at the leading edge as well as in the near wake. At higher AoAs, ( $\alpha > 12^\circ$ ), the separated flow above the flat plate model grew becoming large enough to create a massive wake deficit. The membrane models had a significantly less amount of reverse flow present, resulting in a considerably less wake deficit. Comparing both membrane

models, the 1 percent pre-tension membrane showed a slight improvement in both a smaller separation bubble and wake deficit compared to the 4 percent pre-tension model. This slight improvement was also seen in the force data obtained by Zhang et al. [36].

The Reynolds shear stress term and U-RMS fluctuations provided insight on both momentum transport and shear layer growth. At low AoAs ( $\alpha < 12^\circ$ ) the membrane models had a slight decrease in shear layer size compared to the flat plate case. At larger AoAs, membrane models continued to have a smaller shear layer size as well as in increase momentum transport and turbulent mixing.

Analysis of the membrane's deflections led to the following trends, as AoA was increased the mean deflection (averaged camber) also increased. While the 1 percent pre-tension membrane had greater deflections throughout all AoA, at higher AoA both membrane model deflections leveled off where the models seem to have reached their material limits. A similar trend was also found in the frequency which the membranes oscillate at. Frequencies increased with AoA where the 4 percent pre-tension membrane generally vibrated at a higher frequency throughout the AoAs. Eventually, the frequencies leveled off and started to decrease at the higher AoA. RMS fluctuations shared similar experiences, as AoA was increased the fluctuations also increased. However, the fluctuations quickly subsided as the AoA was increased to higher angles. In preliminary results the outer asymmetric deflections were thought to be a byproduct of both wing tip vortices and mounting hardware effects. Final results show mounting hardware had no major effect on the asymmetric deflections however fluctuations did increase at the outer membranes when the center mounting hardware was used.

The synchronized experiments were able to provide highlights in the coupled membrane and flow interactions. Comparisons of the membrane's dominate frequency to the flow-field's dominate frequency showed the membrane's ability to influence the surrounding flow. There is a dependency on location within the flow-field, however flows approximately close to the trailing edge and near wake had apparent membrane fluctuations present. Examination of the instantaneous vortices shows the membrane's ability to produce a positive vortex structure at the trailing edge. These structures introduced higher momentum fluid in the near wake aiding in a more favorable wake. While FSIs were present at all AoAs, angles at which the membrane's fluctuations were substantial produced superior interactions.

The membrane's wave like motion was analyzed and found to be a combination of a traveling wave and standing wave. A high pressure bulge would develop at the leading edge of the membrane. This bulge would then traverse down the membrane where at an approximate location of  $x/c = 0.65$  the membrane would transition to a standing wave and release the higher momentum fluid into the trailing edge. Wave speed was shown to be a function of pre-tension and AoA. The higher pre-tension membrane allowed a faster wave propagation compared to the lower pre-tension model. The aerodynamic loading associated with increasing AoA was also thought to increase the wave speed.

### **Future Investigation**

This study was a continuation of previous research to further understand the fluid structure interactions, particularly within this investigation, of a low aspect ratio flexible membrane wing. Membrane models showed signs of highly 3D deflections as well as asymmetric deflections, while the flow results showed a strong dependence on

membrane oscillations. Both of these features enlighten some aspect of the FSIs, however there is much that is left unanswered.

Future studies can incorporate streamwise stereo PIV as well as spanwise 3-component PIV measurements. These measurements can examine the presence of spanwise flow as well as the interactions between membrane cells and battens. Furthermore, an investigation on how the outer membranes interact with the wing tips vortices can be studied. Different planes of spanwise stereo PIV can be conducted to see the evolution of the membrane's interactions. To better link experimental results with numerical studies a Dynamic Mode Decomposition (DMD) can be conducted on past and/or current data to generate a low order predictive model, where these models could be used to help validate current fluid structure solvers. While this study as well as others have provided more knowledge of low Reynolds number flight of passively compliant wings, there is still much that is not well understood about the fluid structure interactions.

## APPENDIX A 2D PIV UNCERTAINTY

Bias uncertainty in the PIV velocity measurement is obtained by computing the root-sum-square of the individual uncertainties used to determine velocity as explained by Coleman and Steele [50]. The velocity obtained by each interrogation area is measured via Equation A-1, where  $\Delta t$  is the time interval between laser pulses,  $L_p$  is the pixel width of the calibration target,  $D$  is the particle displacement, and  $L_m$  is the measured width of the calibration target.

$$|v| = \frac{DL_m}{L_p\Delta t} \quad \text{A-1}$$

The bias uncertainty is shown in equation A-2, where the  $\theta$  terms represent the partial derivatives of Equation A-1 (the magnitude of velocity) taken with respect to the denoted subscripted variables. These terms are better known as the absolute sensitivity coefficients. The  $B$  terms represent the uncertainty in each measurement denoted by the subscripted variable.  $B_D$  is the bias uncertainty of the particle displacement.  $B_{L_m}$  is the bias uncertainty in the physical width (resolution of the device used to measure the distance).  $B_{L_p}$  is the bias uncertainty in pixel width of the calibration image. Lastly,  $B_{\Delta t}$  is the bias uncertainty in the time between laser pulses. It should be noted that this method does not account for incorrect PIV vectors that were not removed by outlier rejection. The random uncertainty, Equation A-3, follows that provided by Coleman and Steele [50]. Where the total uncertainty is obtain by computing the root-sum-square of both the bias uncertainty and random uncertainty.

$$B_{|v|} = \left[ (\theta_D B_D)^2 + (\theta_{L_m} B_{L_m})^2 + (\theta_{L_p} B_{L_p})^2 + (\theta_{\Delta t} B_{\Delta t})^2 \right]^{\frac{1}{2}} \quad \text{A-2}$$

$$R = \frac{\sigma}{\sqrt{n}} \quad \text{A-3}$$

## APPENDIX B VIBRATIONAL ANALYSIS

In the set-up for the independent DIC experiments a new mounting arm needed to be constructed. During construction of the mount, the question of whether the frequency at which the mounting arm vibrates would influence the membrane's fluctuations was proposed. This led into a vibrational analysis to obtain the mounting hardware's frequency. A PCB Piezotronics triaxial accelerometer was adhered to the back of one support hanger shown in Figure B-1, where the membrane was removed prior to testing. The accelerometer was positioned such that the x-axis pointed in the spanwise direction, the y-axis pointed normal to the tunnel's floor and the z-axis pointed in the streamwise direction. Initial testing showed the mounting arm having spikes in frequency at 64, 85, and 128 Hz, Figure B-2 plots the PSD for all three axes of the accelerometer. This frequency was undesirable due to its relation to the membrane's frequency, where the membrane's frequencies typically ranged from 50 Hz – 90 Hz. After further investigations where the accelerometer was adhered to the sidewall of the tunnel, it was found that the 64 Hz obtained in the mounting arm was actually being transferred from the tunnel. The 85 Hz was found to be the natural frequency of the mounting arm itself. Figure B-3 plots the PSD for the accelerometer attached to the sidewall. After numerous different configurations, the design of the mounting arm was changed. This time the mount would be supported by an 80/20<sup>®</sup> stand positioned next to the side wall. This would allow the mounting arm to be cantilevered into the ELD-WT while not actually making contact with the sidewall. Figure B-4 plots the PSD of the cantilevered mounting arm. The new design not only shifted the frequency experienced

within the mount, it also stiffened the mount producing a lower overall power for the accelerations experienced in each direction.

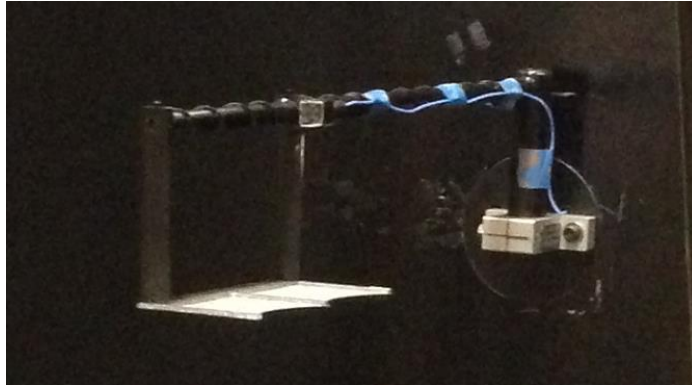


Figure B-1. Accelerometer attached to the back of mounting arm. Photo courtesy of author.

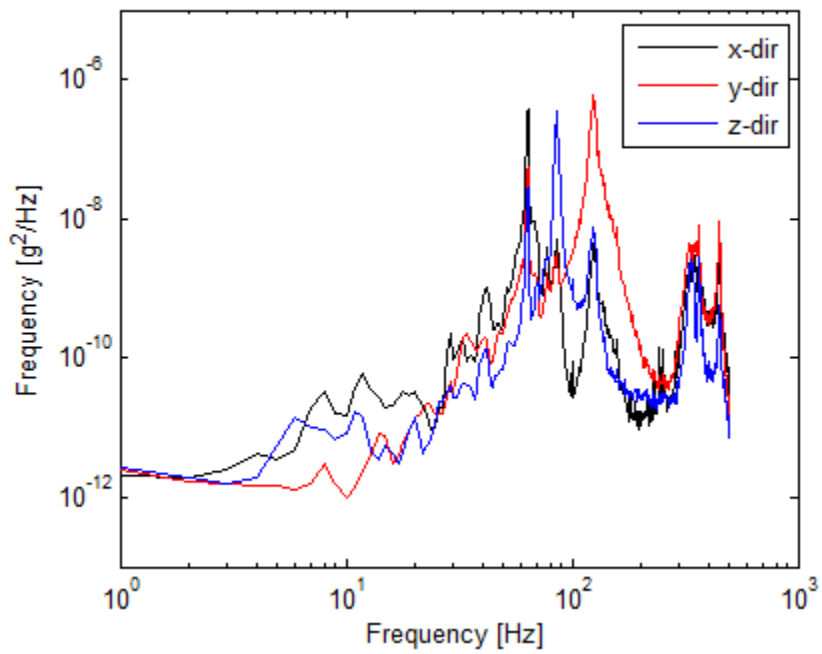


Figure B-2. PSD of original mounting arm.

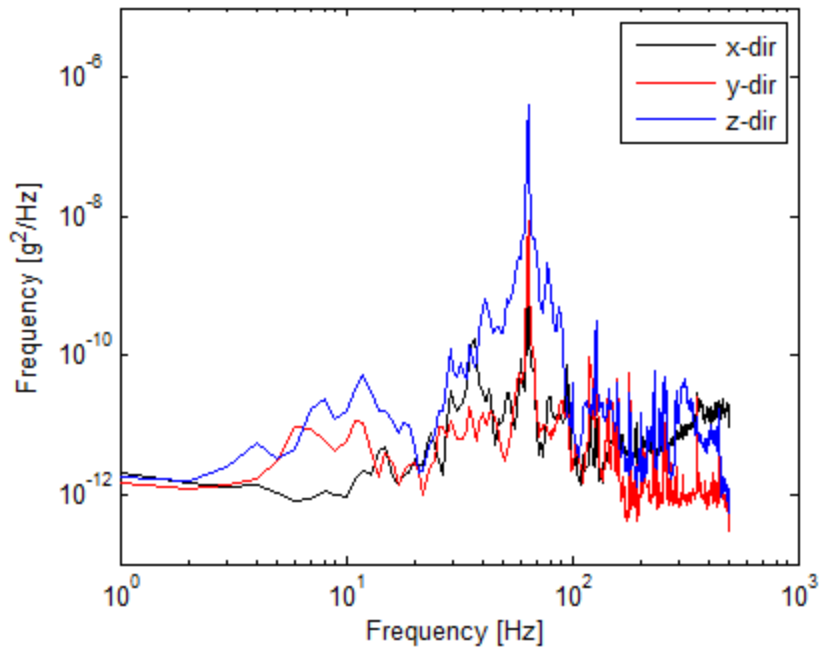


Figure B-3. PSD of ELD-WT.

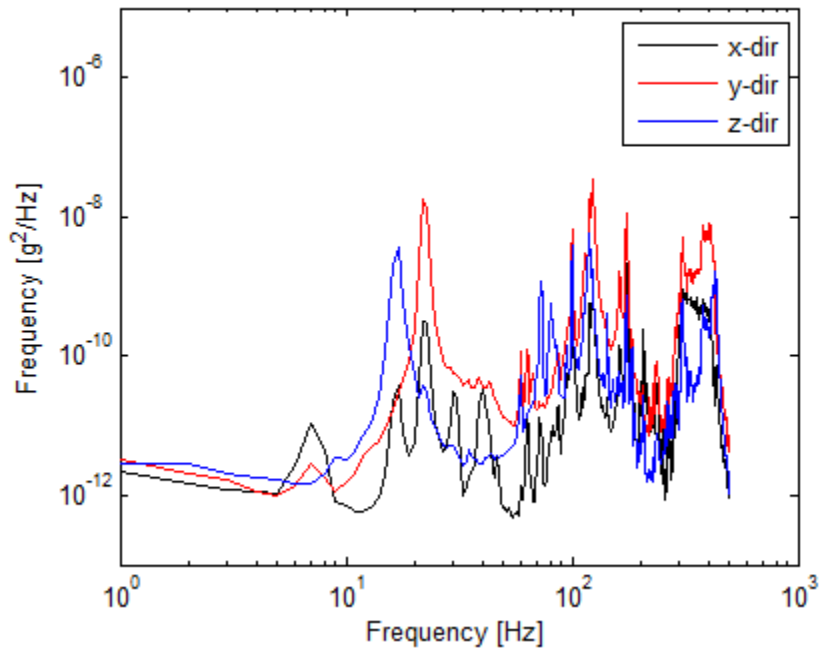


Figure B-4. PSD of cantilevered mounting arm.

## LIST OF REFERENCES

- [1] K. L. Bishop, "The relationship between 3-D kinematics and gliding performance in the southern flying squirrel, *Glaucomys volans*," *Journal of Experimental Biology*, vol. 209, no. Pt 4, pp. 689–701, Feb. 2006.
- [2] S. Swartz, J. Iriarte-Diaz, D. Riskin, and A. Song, "Wing structure and the aerodynamic basis of flight in bats," *American Institute of Aeronautics and Astronautics Aerospace Sciences*, pp. 1–10, 2007.
- [3] D. K. Riskin, D. J. Willis, J. Iriarte-Díaz, T. L. Hedrick, M. Kostandov, J. Chen, D. H. Laidlaw, K. S. Breuer, and S. M. Swartz, "Quantifying the complexity of bat wing kinematics," *Journal of Theoretical Biology*, vol. 254, no. 3, pp. 604–15, Oct. 2008.
- [4] W. Shyy, M. Berg, and D. Ljungqvist, "Flapping and flexible wings for biological and micro air vehicles," *Progress in Aerospace Sciences*, vol. 35. 1999.
- [5] U. Norberg and Y. Winter, "Wing beat kinematics of a nectar-feeding bat, *Glossophaga soricina*, flying at different flight speeds and Strouhal numbers," *Journal of Experimental Biology*, vol. 209, no. 19, pp. 3887–3897, Oct. 2006.
- [6] X. Tian, J. Iriarte-Diaz, K. Middleton, R. Galvao, E. Israeli, A. Roemer, A. Sullivan, A. Song, S. Swartz, and K. Breuer, "Direct Measurements of the Kinematics and Dynamics of Bat Flight," *Bioinspiration & Biomimetics*, vol. 1, no. 4, pp. S10–8, Dec. 2006.
- [7] A. Song, X. Tian, E. Israeli, R. Galvao, K. Bishop, S. Swartz, and K. Breuer, "Aeromechanics of Membrane Wings with Implications for Animal Flight," *AIAA J.*, vol. 46, no. 8, pp. 2096–2106, Aug. 2008.
- [8] P. G. Ifju, D. A. Jenkins, S. Ettinger, Y. Lian, W. Shyy, and M. R. Waszak, "Flexible-Wing-Based Micro Air Vehicles," *40th AIAA Aerospace Sciences Meeting*, pp. 1-13, 2002.
- [9] W. Shyy, F. Klevebring, M. Nilsson, J. Sloan, B. Carroll, and C. Fuentes, "Rigid and Flexible Low Reynolds Number Airfoils," *Journal of Aircraft*, vol. 36, no. 3, pp. 523–529, May 1999.
- [10] Y. Lian and W. Shyy, "Laminar-Turbulent Transition of a Low Reynolds Number Rigid or Flexible Airfoil," *AIAA Journal*, vol. 45, no. 7, pp. 1501–1513, Jul. 2007.
- [11] P. B. S. Lissaman, "Low-Reynolds-Number Airfoils," *Annual Review of Fluid Mechanics*, vol. 15, no. 1, pp. 223–239, Jan. 1983.

- [12] M. Gaster, "The Structure and Behaviour of Laminar Separation Bubbles," *Aeronautical Research Council Reports and Memoranda*, no. 3595. 1967.
- [13] B. Thwaites, "The Aerodynamic Theory of Sails," *Proceedings of the Royal Society of London. Series A, Mathematical, Physical and Engineering Sciences*, vol. 261, no. 1306, pp. 402–422, 1961.
- [14] I. M. Kroo, "Aerodynamics, Aeroelasticity, and Stability of Hang Gliders- Experimental results," *National Aeronautic and Space Administration Technical Memorandum*. no. 81269. April, 1981.
- [15] G. M. Maneia, "Aerodynamic study of airfoils and wings for power kites applications," October 2007.
- [16] P. G. Ifju, S. Ettinger, D. Jenkins, and L. Martinez, "Composite materials for Micro Air Vehicles," *SAMPE conference*, pp. 1-12, May. 2001.
- [17] B. Stanford, P. Ifju, R. Albertani, and W. Shyy, "Fixed membrane wings for micro air vehicles: Experimental characterization, numerical modeling, and tailoring," *Progress in Aerospace Sciences*, vol. 44, no. 4, pp. 258–294, May 2008.
- [18] P. Rojratsirikul, Z. Wang, and I. Gursul, "Unsteady Fluid–Structure Interactions of Membrane Airfoils at Low Reynolds Numbers," *Experiments in Fluids*, vol. 46, no. 5, pp. 859–872, Feb. 2009.
- [19] P. Rojratsirikul, Z. Wang, and I. Gursul, "Effect of pre-strain and excess length on unsteady fluid–structure interactions of membrane airfoils," *Journal of Fluids and Structures*, vol. 26, no. 3, pp. 359–376, Apr. 2010.
- [20] P. Rojratsirikul, M. S. Genc, Z. Wang, and I. Gursul, "Flow-induced vibrations of low aspect ratio rectangular membrane wings," *Journal of Fluids and Structures*, vol. 27, no. 8, pp. 1296–1309, Nov. 2011.
- [21] R. E. Gordnier and M. R. Visbal, "Implicit LES Computations with Applications to Micro Air Vehicles," *DoD High Performance Computing Modernization Program Users Group Conference*, pp. 73–80, Jun. 2009.
- [22] H. Hu, M. Tamai, and J. T. Murphy, "Flexible-Membrane Airfoils at Low Reynolds Numbers," *Journal of Aircraft*, vol. 45, no. 5, pp. 1767–1778, Sep. 2008.
- [23] R. Smith and W. Shyy, "Computation of aerodynamic coefficients for a flexible membrane airfoil in turbulent flow: A comparison with classical theory," *Physics of Fluids*, vol. 8, no. 12, p. 3346, Aug 1996.
- [24] S. Greenhalgh, "Aerodynamic properties of a two-dimensional inextensible flexible airfoil," *AIAA Journal*, vol. 22, no. 7, pp. 865–870, Jul. 1984.

- [25] T. SUGIMOTO and J. SATO, “Aerodynamic characteristics of two-dimensional membrane airfoils,” *Journal of the Japan Society for Aeronautical and Space Sciences*, vol. 36; no.409; pp.86-93, 1988.
- [26] B. G. Newman and H. T. Low, “Two-dimensional impervious sails: experimental results compared with theory,” *Journal of Fluid Mechanics*, vol. 144, pp. 445–462, Jul. 1984.
- [27] R. Smith and W. Shyy, “Computation of unsteady laminar flow over a flexible two-dimensional membrane wing,” *Physics of Fluids*, vol. 7, no. 9, p. 2175, May 1995.
- [28] J. W. Johnston, W. Romberg, P. J. Attar, and R. Parthasarathy, “Experimental Characterization of Limit Cycle Oscillations in Membrane Wing Micro Air Vehicles,” *Journal of Aircraft*, vol. 47, no. 4, pp. 1300–1308, Jul. 2010.
- [29] P. J. Attar, B. J. Morris, W. a. Romberg, J. W. Johnston, and R. N. Parthasarathy, “Experimental Characterization of Aerodynamic Behavior of Membrane Wings in Low-Reynolds-Number Flow,” *AIAA Journal*, vol. 50, no. 7, pp. 1525–1537, Jul. 2012.
- [30] N. Mastramico and J. Hubner, “A Study of the Wake Characteristics for Membrane Flat and Cambered Plates,” *26th AIAA Aerodynamic Measurement Technology and Ground Testing Conference*, pp. 1–13, 2008.
- [31] J. P. Hubner and T. Hicks, “Trailing-edge scalloping effect on flat-plate membrane wing performance,” *Aerospace Science and Technology*, vol. 15, no. 8, pp. 670–680, Dec. 2011.
- [32] K. D. Scott, J. P. Hubner, and L. Ukeiley, “Cell Geometry and Material Property Effects on Membrane and Flow Response,” *AIAA Journal*, vol. 50, no. 3, pp. 755–761, Mar. 2012.
- [33] Y. J. Abudaram, P. G. Ifju, J. P. Hubner, and L. Ukeiley, “Controlling Pre-Tension of Silicone Membranes on Micro Air Vehicle Flexible Wings,” *AIAA 50th Aerospace Sciences Meeting*, pp. 1–11, Jan 2012.
- [34] A. Timpe, L. Ukeiley, and Z. Zhang, “Flow and Structure Measurements of a Passively Compliant Wing,” *AIAA 50th Aerospace Sciences Meeting*, pp. 1–22, Jan 2012.
- [35] A. Timpe, Z. Zhang, J. P. Hubner, and L. Ukeiley, “Passive flow control by membrane wings for aerodynamic benefit,” *Experiments in Fluids*, vol. 54, no. 3, p. 1471, Feb. 2013.

- [36] Z. Zhang, J. P. Hubner, A. Timpe, L. Ukeiley, Y. Abudaram, and P. Ifju, "Effect of Aspect Ratio on Flat-Plate Membrane Airfoils," *AIAA 50th Aerospace Sciences Meeting*, pp. 1–15, Jan. 2012.
- [37] R. Albertani, P. Khambatta, A. Hart, L. Ukeiley, M. Oyarzun and L. Cattafesta, "Validation of a low Reynolds number aerodynamic characterization facility," *47th AIAA Aerospace Sciences Meeting*, pp. 1-10, Jan. 2009.
- [38] M. Sytsma, "Aerodynamic Flow Characterization of Micro Air Vehicles Using Flow Visualization Methods," 2006.
- [39] DantecDynamics, "DynamicStudio v3.12 User's Guide."
- [40] CorrelatedSolutions, "Vic-3D 2010 Testing Guide," 2010.
- [41] J. Griffin, T. Schultz, R. Holman, L. S. Ukeiley, and L. N. Cattafesta, "Application of multivariate outlier detection to fluid velocity measurements," *Experiments in Fluids*, vol. 49, no. 1, pp. 305–317, Apr. 2010.
- [42] J. S. Bendat and A. G. Piersol, *Random Data: Analysis and Measurement Procedures*, 4<sup>th</sup> Edition. Hoboken, NJ, USA: John Wiley & Sons Inc., 2010.
- [43] S. Pope, *Turbulent flows*, Cambridge, United Kingdom: Cambridge University Press, 2000.
- [44] G. E. Torres and T. J. Mueller, "Low aspect ratio aerodynamics at low Reynolds numbers," *AIAA Journal.*, vol. 42, no. 5, May 2004.
- [45] Y.-C. Liu and F.-B. Hsiao, "Aerodynamic Investigations of Low-Aspect-Ratio Thin Plate Wings at Low Reynolds Numbers," *Journal of Mechanics*, vol. 28, no. 01, pp. 77–89, Mar. 2012.
- [46] R. L. Panton, *Incompressible flow*, 3<sup>rd</sup> Edition. Hoboken, NJ, USA: John Wiley & Sons Inc., 2005.
- [47] Z. Zhang, N. Martin, A. Wrist, and J. Hubner, "Force and Deformation Measurement of Low Aspect Ratio Membrane Airfoils," *AIAA 51th Aerospace Sciences Meeting*, pp. 1–17, Jan. 2013.
- [48] D. E. Calderon, Z. Wang, I. Gursul, and M. R. Visbal, "Volumetric measurements and simulations of the vortex structures generated by low aspect ratio plunging wings," *Physics of Fluids*, vol. 25, no. 6, June 2013.
- [49] A. Fage and F. C. Johansen, "On the Flow of Air behind an Inclined Flat Plate of Infinite Span," *Proceedings of the Royal Society A: Mathematical, Physical and Engineering Sciences*, vol. 116, no. 773, pp. 170–197, Sep. 1927.

- [50] H. W. Coleman and W. G. Steele, *Experimentation, Validation, and Uncertainty Analysis for Engineers*, 3<sup>rd</sup> Edition. Hoboken, NJ, USA: John Wiley & Sons Inc., 2009.

## BIOGRAPHICAL SKETCH

As a child, Alex Arce was always interested in the way things operated. This resulted in discussions with his mother asking “why do you always take apart your toys?” Alex would always replay “because I want to know how it works”. This interest continued to follow Alex all the way through high school. After graduating, Alex enrolled in an auto mechanic trade school. At the end of the 14 months of training he graduated and obtained a job at an auto collision repair shop. During this time Alex enjoyed working on automobiles however he wasn’t completely convinced this was the lifestyle he wanted.

Alex continued working while he enrolled at a local community college where he earned his Associate of Arts degree. Upon completion in 2008, Alex was accepted to the University of Florida as a transfer student within the mechanical and aerospace department. During his time as an undergraduate student, Alex joined the UF’s men’s novice rowing team, where later he then joined the varsity team. In the beginning of his senior year, Alex decided to volunteer his free time in a fluids lab. After a few months he was offered an undergraduate research position, this is where he started to find an appreciation for research. In fall 2011, Alex graduated with a dual Bachelor of Science in both mechanical and aerospace engineering. In spring 2012, he started his graduate degree under the guidance of Dr. Lawrence Ukeiley. Alex continues to conduct research and expects to graduate with a Master of Science in aerospace engineering in December 2013.